Geochemistry of Late Permian basalts from boreholes in the Sichuan Basin, SW China: Implications for an extension of the Emeishan large igneous province

Xiaoyu Liu [a,b], Nansheng Qiu [a,b,*], Nina Søager [c], Xiaodong Fu [d], Ran Liu [a,b,e]

[a] State Key Laboratory of Petroleum Resources and Prospecting, China University of Petroleum, Beijing 102249, China
[b] College of Geosciences, China University of Petroleum, Beijing 102249, China
[c] Department of Geosciences and Natural Resource Management, University of Copenhagen, Copenhagen 1350, Denmark
[d] PetroChina Hangzhou Research Institute of Geology, Hangzhou 310023, China
[e] Research Institute of Exploration and Development, Southwest Oil & Gas Field Branch Company, PetroChina, Chengdu 610041, China

ARTICLE INFO

ABSTRACT

The emplacement of the Late Permian Emeishan large igneous province (ELIP) in the Upper Yangtze craton, SW China, is considered to be a crucial factor that triggered the end-Guadalupian biodiversity crisis. However, the contribution of ELIP remains debated because of its relatively modest known size. The restricted assessment of its areal extent is, in part, due to the lack of study of the potential volcanic rocks concealed beneath younger strata. Here we present the first geochemical and isotopic variations and detailed spatial distribution of Late Permian basaltic rocks penetrated by deep exploratory boreholes in the Sichuan Basin. The Late Permian basaltic rocks are mainly distributed in the western and northeastern parts of the Sichuan Basin and are positioned at the same stratigraphic level as the Emeishan flood basalts. Petrography, whole-rock trace elements and Sr-Nd-Pb isotopic compositions demonstrate that these rocks are alkaline basalts and have oceanic island basalt - like characteristics, indicating a similar origin as the Emeishan flood basalts. The trace element and isotope ratios suggest that the basaltic magmas in the western Sichuan Basin were derived by low degrees of partial melting of a garnet-bearing source. In contrast, the basalts in the northeastern part of the basin were generated by higher degrees of melting of a shallower mantle source in the spinel-garnet transition zone. Varying amounts of contamination by lower continental crustal melts are suggested by rough correlations between isotope and immobile trace element ratios. The spatial changes in composition and origin of the basaltic rocks in the Sichuan Basin can be interpreted as the result of varying extents of Emeishan mantle plume-lithosphere interaction under different lithospheric stress backgrounds, such that the reactivation of pre-existing basement faults controlled the emplacement of basaltic magma in the periphery of the ELIP. Our work reveals a substantially broader extent of the ELIP in buried sedimentary strata, which might have contributed to the abrupt end-Guadalupian climatic change.

1. Introduction

Large igneous provinces (LIPs) represent rapid production of anomalous and voluminous intraplate magmatism and are generally linked with high-temperature mantle plumes rising from the deep interior of the Earth and upwelling beneath the base of the lithosphere (e.g., Richards et al., 1989; Campbell and Griffiths, 1990; Campbell, 2005). As the largest magma outpourings recorded on our planet (Bryan and Ernst, 2008, Bryan and Ferrari, 2013), the emplacement of both extrusive and intrusive igneous rocks of LIPs can cover vast areas (typically $>10^5$ km^2) within short durations of peak eruptions (<5 Myr; e.g., Ernst, 2014; Schoene et al., 2015). Thereby, they have an important bearing on mineral and hydrocarbon occurrences and play a potential causal role in supercontinent breakup and environmental catastrophes including mass extinction events throughout Earth's history (e.g., Campbell and Griffiths, 1990; Ernst et al., 2005, Ernst and Youbi, 2017; Wignall et al., 2009).

The Permian Emeishan large igneous province (ELIP) in SW China is
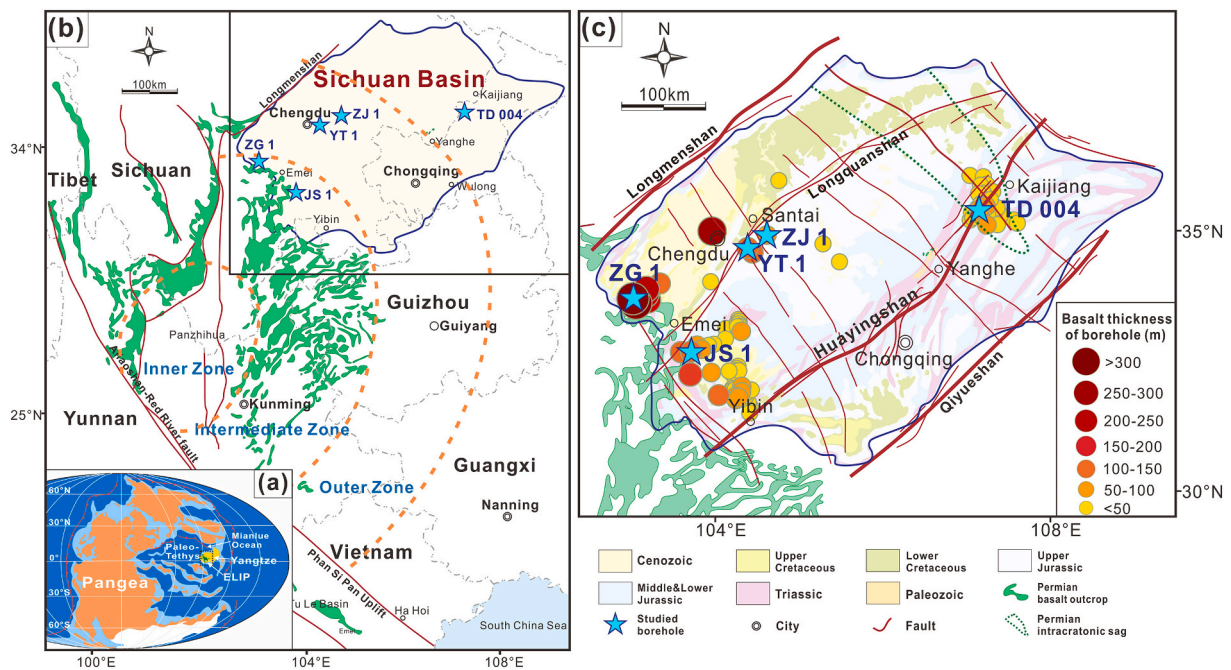

Fig. 1. (a) Global paleogeographic plate reconstruction in Middle-Late Permian (modified from Cocks and Torsvik, 2013). (b) Distribution of the Late-Permian Emeishan flood basalts in SW China with locations of studied boreholes indicated by blue stars (modified from Li et al., 2017; Jiang et al., 2018 and references therein). (c) Map of the Sichuan Basin region, showing the locations and thicknesses of Permian basalts from boreholes and the distribution of major deep-seated faults. The outlines of outcropping strata and faults are modified from Xiong et al. (2015) and Li et al. (2020), respectively. Drilling data are collected from PetroChina and SINOPEC. (For interpretation of the references to colour in this figure legend, the reader is referred to the web version of this article.)

one of the most intensely studied LIPs over the years because it hosts world-class Fe-Ti-V oxide deposits and is contemporaneous with the end-Guadalupian mass extinction event (Zhou et al., 2005, 2008; Wignall et al., 2009; Zhang et al., 2009; Shellnutt, 2014). Numerous investigations on geochemistry (e.g., Xu et al., 2001, 2004, 2007; Zhang et al., 2006; Kamenetsky et al., 2012), geochronology (e.g., He et al., 2007, 2010; Zhong et al., 2014; Huang et al., 2018; Deng et al., 2020; Shellnutt et al., 2020), geophysics (e.g., Xu et al., 2007; Chen et al., 2015, Chen et al., 2017), crustal uplifting (He et al., 2003; Zhu et al., 2018b) and paleoenvironment (e.g., Jerram et al., 2016; Wignall et al., 2009; Zhang et al., 2015; Chen and Xu, 2019; Zhu et al., 2021a, 2021b) of the ELIP have shown that the igneous rocks are likely correlated to a mantle plume (e.g., Xu et al., 2004, 2007; Ali et al., 2010; Shellnutt, 2014). However, the spatial extent and volume of ELIP (~3 × 10^5 km^2, ~3 × 10^5 km^3; Peate and Bryan, 2008; Shellnutt et al., 2020) are relatively dwarf in comparison with other typical LIPs, i.e., Siberian Traps (~7 × 10^6 km^2, ~4 × 10^6 km^3; Ivanov, 2007), Deccan Traps (~2 × 10^6 km^2, ~3 × 10^6 km^3; Sen, 2001) and Central Atlantic Magmatic Province (~1 × 10^7 km^2, ~3 × 10^6 km^3; Marzoli et al., 2018), casting doubts on the causal relationship between the proposed plume scenario and the end-Guadalupian mass extinction. Despite that recent studies have found several scattered Emeishan volcanic-plutonic rocks exposed outside the ELIP, such as the Tubagou basalts in the Baoxing area along the southeastern margin of the Songpan-Ganzi terrane (Li et al., 2016), the Yanghe basalts in the northeastern Sichuan Basin (SCB) (Li et al., 2017) and the Tu Le rhyolite in northern Vietnam (Shellnutt et al., 2020), it is still inadequate to estimate the dimension of the ELIP based on outcrops due to the influence of substantial deformation associated with multi-stage tectonic events in the Mesozoic and Cenozoic and the cover of younger strata (Charvet, 2013; Liu et al., 2021).

Over the past decade, many Permian basaltic rocks were penetrated by deep industrial boreholes in the SCB as the hydrocarbon exploration of ancient marine strata progressed (Fig. 1; Tian et al., 2017). Recent studies have proposed that these basaltic rocks are temporally associated with the eruption of Emeishan flood basalts (Lu et al., 2019; Ma et al.,

2019; Li et al., 2020), indicating that the ELIP may have covered a substantially larger area than previously thought, because those exposed parts have been partially concealed beneath younger strata. Likewise, the reconstruction of paleo-heat flow using both geodynamic modeling (Wang et al., 2018; He, 2020) and thermal indicators (Zhu et al., 2010, 2016, 2018a; Jiang et al., 2018; Xu et al., 2018) displays a significant thermal perturbation (~100 mW/m^2) at the Late Permian in the basin, indicating a potentially larger scale of the ELIP. However, despite numerous studies, systematic geochemical investigations of Permian basaltic rocks recovered from the boreholes are scarce, and their petrogenesis has not yet been addressed in detail. Identifying the mechanism that produced such extensive magmatism in the SCB is crucial for understanding the deep plumbing systems of the ELIP and tectonic evolution of the region.

In this contribution, we outline the spatial distribution of Permian volcanism in the SCB and present new whole-rock major and trace element and Sr-Nd-Pb isotope data for the Permian basalts and dolerites from boreholes in different parts of the basin. Based on these results, we attempt to constrain the nature of magma sources and mantle melting parameters, track the geodynamic setting of these rocks and estimate the spatial extents of the concealed ELIP, yielding a better understanding of the linkage between the Emeishan volcanism and the hydrocarbon occurrence and mass extinction event.

2. Geological background

2.1. Emeishan large igneous province

A comprehensive review of the ELIP was presented by Shellnutt (2014). Most of the ELIP lies on the western edge of the Yangtze Craton, SW China, bounded by the Longmenshan thrust belt to the northwest and the Ailaoshan-Red River fault to the southwest (Fig. 1b). The province was emplaced in the Late Permian (258–259 Ma; Zhong et al., 2014; Huang et al., 2018; Deng et al., 2020) with a short eruption duration for the main part of the province (probably ~1 Ma; Shellnutt
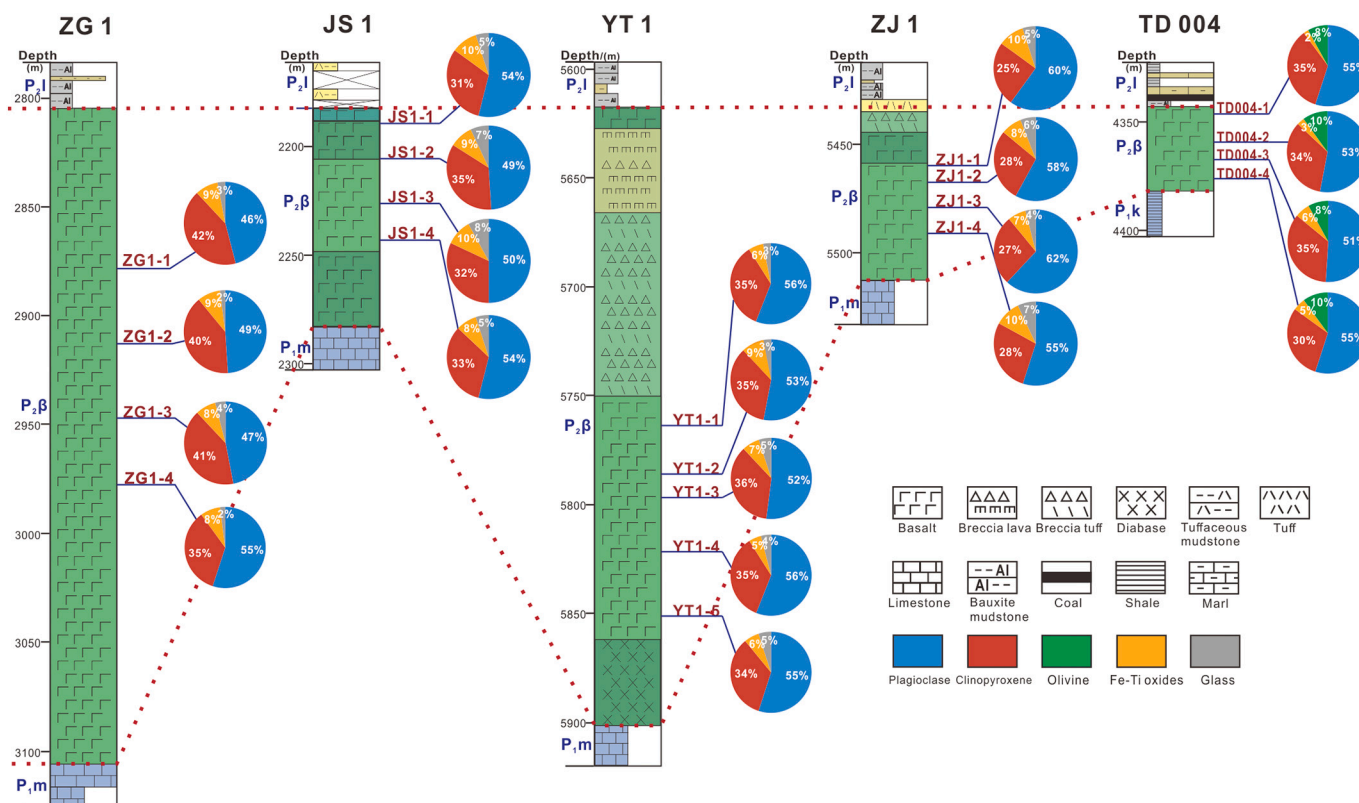
Fig. 2. Stratigraphic correlation of volcanic sequences and modal mineral abundances of studied samples in boreholes across the Sichuan Basin. The scale on the borehole indicates meters below the surface.

et al., 2012, Shellnutt, 2014; Huang et al., 2016; Zhu et al., 2021b) and subsequently dissected by substantial deformation and uplift during the Mesozoic and Cenozoic associated with the collision of the North and South China blocks and the India-Eurasian collision (Chung and Jahn, 1995; Chung et al., 1998; Zhang et al., 2006). The known area of remaining exposed volcanic rocks is considered to cover $\sim 3 \times 10^5$ km^2 from southwest China to North Vietnam with a diameter of ~ 500 km (Fig. 1b; Shellnutt et al., 2020). The province is predominantly composed of flood basalts and contemporaneous felsic plutons, layered mafic-ultramafic intrusions and mafic dyke swarms (Chung and Jahn, 1995; Xu et al., 2001; Shellnutt, 2014; Li et al., 2015). The volcanic sequences in the eastern part of ELIP unconformably overlie the carbonate-dominated Middle Permian Maokou Formation and are, in turn, directly overlain by the Upper Permian terrestrial to marine clastic rocks of the Xuanwei Formation and Longtan Formation (He et al., 2007; Zhong et al., 2014). Based on the erosional state of the Maokou limestone, the province has been structurally subdivided into inner, intermediate, and outer zones (Fig. 1b; He et al., 2003; Xu et al., 2004). The flood basalts of this province are generally further classified into low-Ti and high-Ti geochemical series, which are considered to be located mostly in the inner zone and outer zone, respectively (e.g. Xu et al., 2001, 2004; Xiao et al., 2004). However, the classification scheme of these two series and the clear boundary in spatial and temporal distribution between low-Ti and high-Ti basalts have also been questioned by some scholars (e.g. Hou et al., 2011; Shellnutt and Jahn, 2011; Shellnutt, 2014).

2.2. The Sichuan Basin

The SCB is a polycyclic superimposed sedimentary basin located to the northeast of the ELIP in the northwestern Upper Yangtze Craton with an area of 2.3×10^5 km^2 and it is the main gas-producing region in China (Fig. 1c; Dai et al., 2014; Zhao et al., 2018). Many deep-seated

faults have developed in and around the SCB, particularly the NE-trending Huayingshan Fault, which is the only lithospheric-scale fault cutting across the basin (Fig. 1c; Li, 2020). The basin was formed on the Precambrian crystalline basement and accommodated the lower marine carbonate sequences (from Neoproterozoic to Middle Triassic) and the upper continental clastic sequences (from Late Triassic to Eocene; Liu et al., 2021) with locally intercalated late Paleozoic volcanic rocks (Li et al., 2017; Xia et al., 2020). The pre-Late Triassic marine sequences are the exploration targets and main production strata and contain multiple source rocks (i.e. Upper Sinian mudstone, Lower Cambrian shale, Lower Silurian shale, Upper Permian coal and mudstone; Zou et al., 2014). During the Middle-Late Permian, the basin was dominated by carbonate platform deposits with the development of intra-platform depressions (e.g., Kaijiang-Liangping intracratonic sag; Liu et al., 2021; Huang et al., 2021) in an extensional setting containing Qixia Formation (dolomite, limestone), Maokou Formation (limestone, dolomite) and Longtan For-mation (limestone, shale) from the bottom up (Yang et al., 2020; Feng et al., 2021). Borehole data indicates that the stratigraphic relationships of the Permian volcanic rocks are consistent with those of the eastern part of the ELIP (Fig. 2; Tian et al., 2017; Ma et al., 2019).

3. Samples and analytical methods

3.1. Sample descriptions

The basaltic rocks obtained for this study were collected from five industrial boreholes in the SCB (Fig. 1b, c). Boreholes YT 1 and ZJ 1 are located around the Longquanshan fault and boreholes ZG 1 and JS 1 border the Emei-Yibin fault in the western SCB, while borehole TD 004 is close to the Huayingshan fault in the northeastern SCB (Fig. 1b). The sampling intervals depended on the availability of drill cores and resulted in discontinuous sampling and difficulties in covering complete eruptive cycles. The samples were collected from the central part of the
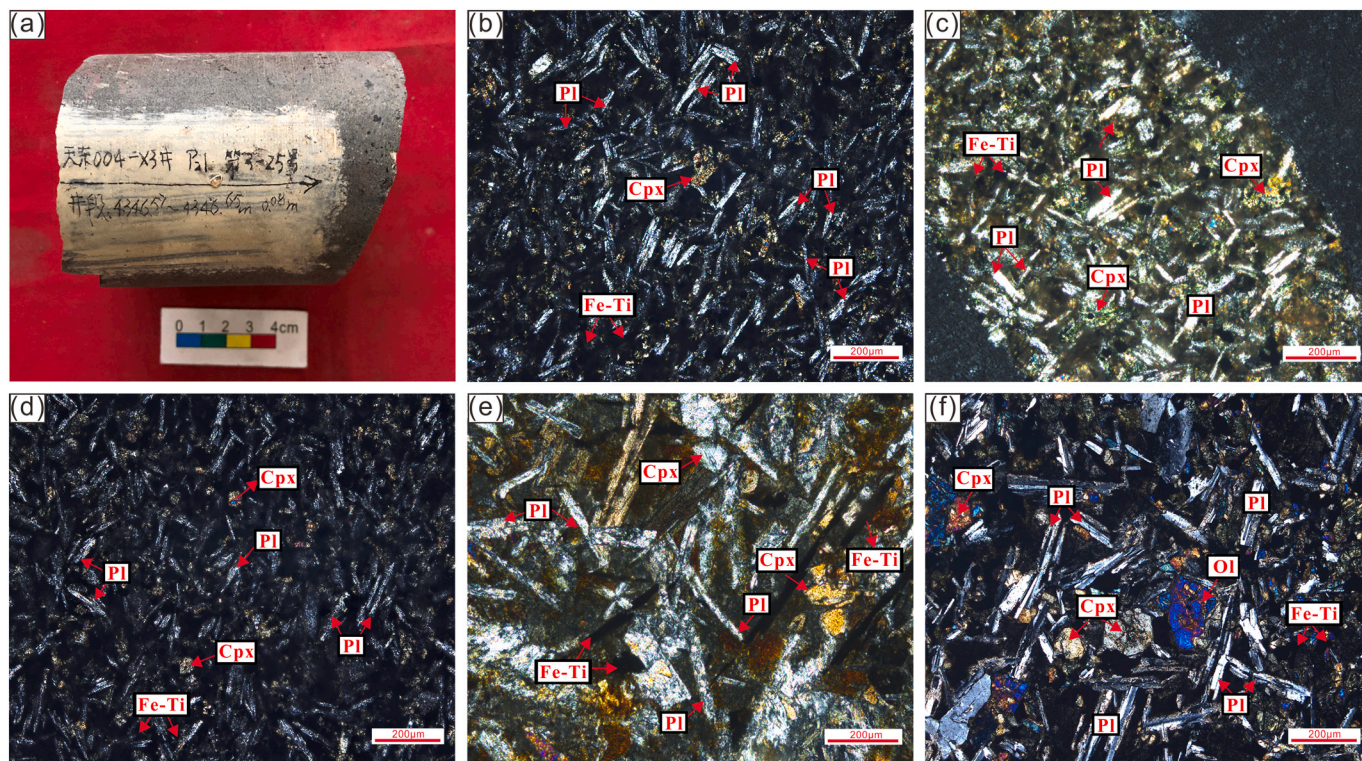
Fig. 3. Representative photographs of basaltic samples from studied boreholes in the Sichuan Basin. Drill core hand specimen from borehole TD 004 at 4346.6 m (a). Thin-section photomicrographs of basalts from boreholes JS 1 (b), ZG 1 (c), ZJ 1 (d) and dolerites from boreholes YT 1 (e) and TD 004 (f) under cross-polarized light. Mineral abbreviations: *Cpx*, clinopyroxene; *Pl*, plagioclase; *Ol*, olivine; and *Fe-Ti*, Fe-Ti oxides.

most massive lava flows with least alteration and amygdules. The depth and modal mineral abundances of samples are shown in Fig. 2. These rocks are overlain by limestone and shale of the Middle Permian Maokou Formation or Kuhfeng Formation (different facies with same deposition age in northeastern SCB), and underlain by bauxite mudstone and shale of the Late Permian Longtan Formation (Fig. 2). The samples from boreholes ZG 1, JS 1 and ZJ 1 are aphyric basalts and have an intergranular or intersertal texture with randomly oriented microcrysts of plagioclase (45–62%), clinopyroxene (25–42%), plus minor Fe-Ti oxides and volcanic glass (Figs. 2 and 3). The samples from boreholes TD 004 and YT 1 are mainly dolerites, showing characteristic interlocking of fine-grained plagioclase (51–56%) and clinopyroxene (30–36%) with a minor amount of olivine, hornblende and Fe-Ti oxides (Figs. 2 and 3).

3.2. Analytical methods

A total of twenty-two volcanic rock samples from studied boreholes in the SCB were crushed into ~200-mesh size using agate mortars for whole-rock major and trace element concentrations, and whole-rock powders (~100 mg) of twelve samples from boreholes YT 1, ZG 1 and TD 004 were selected for Sr-Nd-Pb isotopic analyses. Whole-rock geochemical and Sr-Nd-Pb isotopic analyses were conducted at the Wuhan Sample Solution Analytical Technology Co., Ltd., Wuhan, China. Detailed procedures of the analyses and data processing are described below.

Major element oxides were analyzed on fused glass beads using X-ray fluorescence (XRF) spectrometry using a Primus II instrument (RIGAKU, Osaka, Japan) and ferrous iron was determined by the wet chemical method. Trace element determinations were measured on an Agilent 7700e inductively coupled plasma-mass spectrometer (ICP-MS) (Agilent Technologies, Tokyo, Japan). The detailed procedures of major and trace element compositions are the same as in Xu et al. (2020). The analytical uncertainties for major oxides were better than ~5% and

analytical errors for trace elements were 2–6%. The accuracy of the data was evaluated from the average values of repeated analysis of the standard BHVO-1.

Sr-Nd-Pb isotope analyses were performed on a Neptune Plus multi collector (MC)-ICP-MS instrument (Thermo Fisher Scientific, Dreieich, Germany). The chemical preparations were made on class 100 work benches within a class 1000 over-pressured clean laboratory. The sample powders were acid-leached prior to isotopic analysis following Weis et al. (2005). The detailed methods and instrumentation for Sr-Nd and Pb isotopic measurements are described in Li et al. (2012) and Baker et al. (2004), respectively. Reproducibility and accuracy of Sr-Nd isotope runs were periodically checked by running the Standard Reference Material NBS 987 and Laboratory Standard La Jolla, with a mean $^{87}Sr/^{86}Sr$ ratio of 0.710244 ± 22 (2σ, $n = 32$) and a mean $^{143}Nd/^{144}Nd$ value of 0.512118 ± 15 (2σ, $n = 31$), which are identical within error to their published values (reference data: $^{87}Sr/^{86}Sr = 0.710241 \pm 12$, $^{143}Nd/^{144}Nd = 0.512115 \pm 07$; Thirlwall, 1991; Tanaka et al., 2000, respectively). Measured $^{20x}Pb/^{204}Pb$ ratios were normalized to results of the well-accepted Standard Reference Material NBS 981 values of $^{208}Pb/^{204}Pb = 36.7262 \pm 31$, $^{207}Pb/^{204}Pb = 15.5000 \pm 13$, $^{206}Pb/^{204}Pb = 16.9416 \pm 13$ (Baker et al., 2004). One NBS SRM 981 standard was measured every ten samples analyzed. Analyses of the NBS SRM 981 standard yielded external precisions of 0.03% (2RSD) for $^{20x}Pb/^{204}Pb$ ratios. In addition, the USGS reference material BCR-2 (basalt) yielded results of $^{208}Pb/^{204}Pb = 38.737 \pm 28$, $^{207}Pb/^{204}Pb = 15.628 \pm 3$, $^{206}Pb/^{204}Pb = 18.757 \pm 22$ (2σ, $n = 61$), which is identical within error of 0.03% to their published values (Weis et al., 2006). Total blank levels during the analytical procedure were below 1.22 ng for Sr, 0.05 ng for Nd and 0.36 ng for Pb.
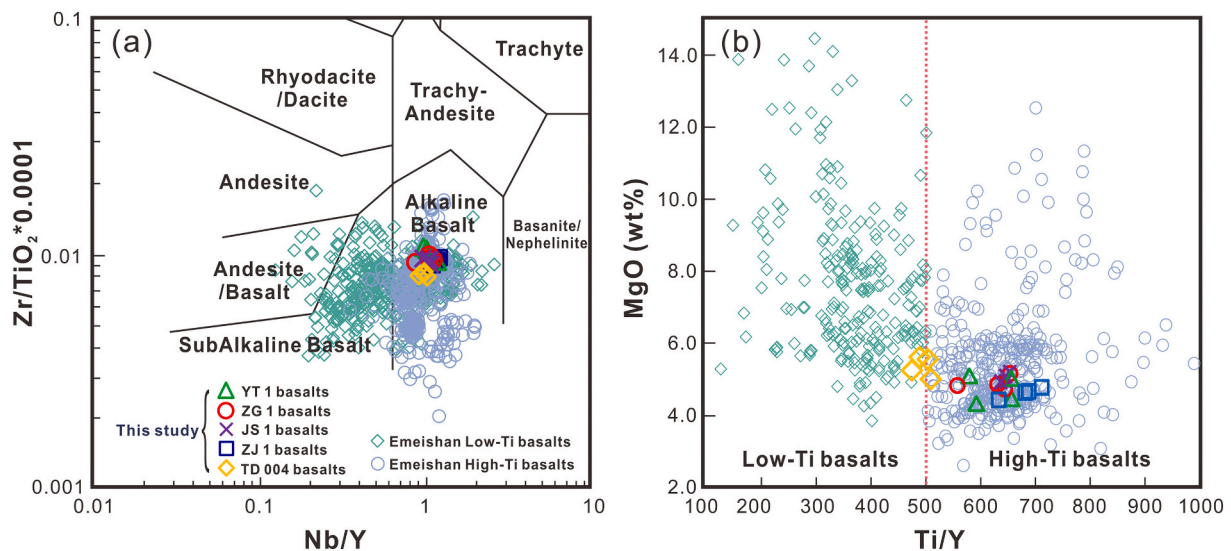
Table 1

Major and trace element abundances of Permian basalts from studied boreholes in SCB.

Borehole	YT 1					ZG 1					JS 1				TD 004				ZJ 1			
Sample no.	YT1-1	YT1-2	YT1-4	YT1-7	YT1-8	ZG1-1	ZG1-2	ZG1-3	ZG1-4	ZG1-5	JS1-1	JS1-2	JS1-3	JS1-4	TD004-1	TD004-2	TD004-3	TD004-4	ZJ1-1	ZJ1-2	ZJ1-3	ZJ1-4
Depth (m)	5763.1	5786.8	5797.2	5821.3	5850.5	2878.1	2913.4	2948.6	2977.1	3001.5	2189.9	2206.8	2227.2	2243.5	4351.8	4360.1	4368.2	4377.5	5460.2	5468.5	5479.9	5492.3
Major elements (wt%)																						
SiO_2	39.96	48.51	48.31	48.22	48.44	48.00	47.14	49.94	49.31	49.40	47.64	49.48	50.17	48.66	46.86	48.30	46.85	46.81	48.46	48.42	47.95	48.37
TiO_2	2.07	3.56	3.38	4.06	4.10	4.01	4.11	3.82	3.85	3.87	3.04	3.19	3.06	3.08	3.04	3.19	3.06	3.08	3.95	3.91	3.78	4.10
Al_2O_3	6.69	13.74	13.89	13.61	13.86	13.25	13.19	13.07	13.47	13.46	13.64	13.30	13.46	13.39	12.75	13.12	13.09	13.26	13.61	13.58	13.68	13.47
Fe_2O_3T	2.89	11.81	12.77	13.17	12.98	14.99	14.50	12.78	13.18	13.18	14.04	13.11	13.14	13.98	16.72	14.76	15.36	15.57	13.05	13.04	13.85	13.76
MnO	0.06	0.15	0.15	0.18	0.18	0.19	0.15	0.16	0.16	0.16	0.15	0.14	0.15	0.14	0.23	0.19	0.19	0.19	0.17	0.17	0.18	0.17
MgO	1.27	4.14	4.90	4.87	4.34	4.67	4.97	4.56	4.72	4.72	5.05	4.79	4.82	4.95	4.93	4.77	5.14	5.20	4.56	4.58	4.37	4.72
CaO	33.87	8.24	7.60	6.56	6.89	6.80	8.71	6.90	8.55	8.57	7.95	7.40	7.31	7.61	8.53	8.63	9.08	8.95	8.44	8.43	8.21	8.57
Na_2O	1.86	3.09	2.72	3.72	3.36	2.96	3.86	2.58	2.06	2.08	3.25	3.09	3.04	3.12	2.77	2.98	2.90	2.91	4.36	3.86	3.52	3.55
K_2O	0.19	1.99	2.09	2.09	2.65	1.46	1.26	2.17	1.30	1.31	0.78	0.84	0.98	0.82	0.28	0.29	0.24	0.25	1.07	1.57	1.63	1.42
P_2O_5	0.25	0.42	0.41	0.43	0.43	0.42	0.45	0.41	0.42	0.43	0.44	0.44	0.44	0.45	0.38	0.40	0.42	0.43	0.41	0.41	0.42	0.43
LOI	8.56	2.49	1.73	2.78	1.99	2.68	2.95	2.99	2.50	2.39	2.75	2.80	2.79	2.70	2.99	3.00	2.99	2.98	2.96	2.74	2.40	2.59
Total	97.68	98.13	97.95	99.69	99.23	99.42	101.28	99.38	99.53	99.55	99.89	99.52	100.42	100.00	99.48	99.63	99.33	99.64	101.04	100.70	99.99	101.15
$Mg^{#}$	29.2	41.0	43.2	42.3	39.9	38.2	40.4	41.4	41.5	41.5	41.6	42.0	42.1	41.2	36.9	39.0	39.9	39.8	40.9	41.0	38.5	40.5
Trace elements (ppm)																						
Sc	6.59	22.8	20.3	23.7	24.4	26.0	27.3	23.8	24.1	23.6	24.8	24.1	24.2	24.5	28.1	28.7	28.9	29.0	23.2	22.8	21.9	24.3
V	109	337	336	372	377	397	404	363	363	366	390	385	385	392	402	403	399	405	376	366	375	368
Cr	58.2	99.0	92.2	62.3	63.8	79.8	83.5	74.1	79.4	79.5	51.9	51.2	50.0	51.9	34.2	33.8	35.6	34.6	61.5	61.7	59.7	64.3
Co	8.2	34.3	42.6	39.6	38.8	42.6	44.2	37.1	39.6	39.9	40.1	39.0	39.4	39.7	50.8	41.9	44.8	45.8	38.9	38.3	38.1	39.2
Ni	19.6	67.6	99.5	80.6	79.4	70.3	70.1	74.4	79.5	81.5	52.4	52.0	50.8	52.1	53.2	47.3	53.3	54.6	81.7	82.2	76.3	84.2
Cu	54	209	230	219	222	198	247	209	206	209	185	208	223	199	248	304	288	289	32	31	32	31
Zn	38	122	126	118	113	127	123	114	118	120	130	124	122	129	150	132	129	131	119	113	114	124
Rb	3.46	49.01	49.92	46.90	57.55	48.01	31.57	76.36	32.36	32.59	22.50	24.78	28.72	26.70	3.00	2.96	2.64	2.75	2.75	2.57	2.66	2.87
Sr	506	739	635	1017	933	436	372	585	502	501	696	708	734	721	508	547	533	542	366	359	355	364
Y	13.75	37.40	35.90	38.72	38.94	44.52	38.87	37.35	38.09	38.26	39.69	39.61	39.76	39.90	39.13	39.20	38.00	38.78	35.46	34.89	36.60	35.20
Zr	114	356	338	374	379	359	374	350	357	356	382	375	380	379	243	254	247	252	356	349	358	351
Nb	11.77	39.08	37.67	42.89	43.37	40.86	43.44	40.19	40.90	41.02	43.06	41.76	39.55	42.20	37.85	40.19	38.11	39.19	41.63	38.81	42.10	39.20
Ta	0.72	2.37	2.33	2.71	2.65	2.45	2.63	2.42	2.46	2.51	2.68	2.51	2.41	2.65	2.16	2.36	2.26	2.34	2.72	2.48	2.67	2.63
Ba	1044	6793	7482	1982	3187	626	346	689	452	451	509	535	663	556	264	281	214	224	58	58	69	85
La	27.02	47.24	45.82	48.21	48.53	45.35	43.25	48.24	46.43	47.18	46.93	47.22	48.88	47.90	34.32	37.83	36.84	38.38	49.93	48.55	48.70	47.60
Ce	48.90	103.41	101.32	108.61	106.71	100.88	98.44	104.25	103.53	104.36	105.76	103.95	107.60	102.00	74.38	79.59	77.96	79.25	106.98	104.14	108.00	101.00
Pr	5.49	12.99	12.78	13.57	13.76	12.67	12.82	13.20	13.18	13.18	13.29	13.16	13.59	13.40	9.05	9.73	9.48	9.66	13.78	13.33	13.10	13.50
Nd	22.53	55.50	53.68	57.91	59.25	53.60	55.40	56.46	56.83	56.23	57.19	57.03	57.62	57.40	38.15	40.78	40.18	41.31	57.90	56.06	58.90	57.10
Sm	4.55	11.68	11.45	12.15	12.23	11.43	11.66	11.56	11.65	11.55	11.64	11.51	11.90	11.70	8.34	8.95	8.73	9.01	12.29	12.09	12.10	12.00
Eu	1.60	3.50	3.33	3.15	3.48	3.30	3.41	3.14	3.12	3.19	3.42	3.24	3.42	3.37	2.31	2.54	2.50	2.79	3.76	3.57	3.42	3.66
Gd	4.83	10.45	9.93	10.44	10.18	10.75	9.88	9.64	9.83	9.92	10.10	10.13	10.45	10.20	7.69	8.25	7.94	8.11	10.08	9.79	10.20	10.00
Tb	0.50	1.39	1.33	1.44	1.37	1.52	1.39	1.31	1.34	1.36	1.45	1.48	1.52	1.39	1.19	1.34	1.22	1.29	1.36	1.35	1.53	1.37
Dy	2.85	7.85	7.45	8.02	7.92	8.65	8.06	7.54	7.79	7.76	8.31	7.80	8.29	7.99	7.45	7.63	7.20	7.60	7.90	7.60	7.83	7.57
Ho	0.48	1.40	1.30	1.45	1.41	1.60	1.47	1.42	1.39	1.41	1.41	1.44	1.44	1.39	1.33	1.43	1.37	1.38	1.34	1.26	1.39	1.37
Er	1.32	3.65	3.49	3.82	3.72	4.17	3.72	3.60	3.67	3.64	3.73	3.67	3.70	3.72	3.84	3.88	3.74	3.91	3.61	3.34	3.45	3.55
Tm	0.17	0.47	0.45	0.52	0.51	0.56	0.50	0.47	0.50	0.49	0.49	0.47	0.48	0.51	0.52	0.53	0.51	0.53	0.45	0.44	0.51	0.47
Yb	0.99	2.92	2.79	3.06	3.07	3.27	3.01	2.98	3.00	2.99	3.12	3.02	3.13	2.98	3.45	3.51	3.33	3.46	2.75	2.70	2.79	2.89
Lu	0.16	0.42	0.39	0.43	0.44	0.45	0.43	0.42	0.43	0.42	0.43	0.43	0.44	0.45	0.50	0.49	0.49	0.50	0.41	0.39	0.43	0.49
Hf	2.76	9.09	8.53	9.59	9.57	8.97	9.02	9.02	9.13	9.29	9.37	8.98	9.08	8.57	5.86	6.05	5.92	6.38	9.17	8.94	9.08	8.85
Pb	15.43	24.6	15.5	6.48	6.43	6.85	17.7	8.05	8.31	8.21	7.45	7.42	7.06	7.37	5.69	4.75	5.05	5.12	5.95	5.98	5.89	6.11
Th	2.48	7.44	7.14	7.48	7.77	6.98	7.33	7.61	7.53	7.75	7.04	6.89	7.09	7.00	5.27	5.51	5.36	5.56	7.25	7.06	6.95	7.34
U	1.30	1.84	1.83	1.72	1.82	1.64	1.69	1.75	1.78	1.72	1.62	1.61	1.61	1.59	1.19	1.25	1.21	1.25	1.34	1.29	1.46	1.35

LOI: weight loss on ignition to 1000 °C. $Mg^{#} = Mg^{2+}/(Mg^{2+}+Fe^{2+})$ in atomic ratio, assuming 15% of total iron oxide is ferric.

Fig. 4. Diagrams of (a) $Zr/TiO_2 \times 0.0001$ vs. Nb/Y (after Winchester and Floyd, 1977) and (b) MgO vs. Ti/Y for the basaltic samples in the Sichuan Basin. Literature data of Emeishan low-Ti and high-Ti basalts came from GEOROC database (http://georoc.mpch-mainz.gwdg.de/georoc/). The boundary of Emeishan low-Ti and high-Ti basalts (pink dashed line) is from Xu et al. (2001). (For interpretation of the references to colour in this figure legend, the reader is referred to the web version of this article.)

4. Results

4.1. Whole-rock major and trace elements

The concentrations of major and trace elements of the studied lava samples are listed in Table 1 and illustrated in Figs. 4 and 5. The samples show some degree of alteration in thin sections, so the whole-rock raw data has been normalized to 100% on a volatile-free basis by correcting for LOI, and the sample YT1–1 was discarded in this study due to the high LOI value (8.56 wt%). We use the normalized values in the following discussions.

All of the rocks have a narrow range of major oxide compositions and have SiO_2 = 46.81–50.17 wt%, Al_2O_3 = 12.75–13.89 wt%, CaO = 6.56–9.08 wt%, P_2O_5 = 0.38–0.45 wt%, high $Fe_2O_3^T$ = 11.81–16.72 wt % and total alkali contents ($Na_2O + K_2O$ = 3.05–6.01 wt%). The $Mg^{\#}$ values of the samples range from 36.9 to 43.2 with MgO contents of 4.14–5.20 wt%, indicative of evolved magmas. On the Nb/Y vs. Zr/TiO_2 diagram, all of the samples plot in the field of alkaline basalts (Fig. 4a). The Emeishan continental flood basalts are commonly divided into high-Ti (Ti/Y > 500) and low-Ti (Ti/Y < 500) series (Xu et al., 2001). Our data show that the samples from the western SCB belong to the high-Ti series (Ti/Y = 558–709), which is a notable character of the outer zone of ELIP (e.g., Han et al., 2009; Liao et al., 2012; Li et al., 2017), whereas the samples from borehole TD 004 display moderate Ti/Y ratios (483–505) (Fig. 4b; published data from GEOROC database; http://georoc.mpch-mainz.gwdg.de/georoc/).

All of the samples show uniform chondrite-normalized rare earth element (REE) patterns with apparent enrichment in LREEs and no or slightly negative Eu anomalies (Eu/Eu* = 0.84–1.00; Fig. 5a). Among these, the rocks from borehole TD 004 show relatively less LREE enrichment (($La/Yb)_N$ = 7.13–7.96) and HREE depletion (($Dy/Yb)_N$ = 1.84–1.98) than those of other boreholes (($La/Yb)_N$ = 9.95–13.02; ($Dy/Yb)_N$ = 2.67–3.03). Among the trace elements, mobile elements (e.g., Rb, Ba, Sr and K) display considerable variability relative to the alteration-resistant immobile elements such as Th, Nb, Zr and P (all incompatible in basaltic melts in early crystallizing phases). Especially the large negative anomalies of Rb and K in borehole TD 004 and ZJ 1, as well as the positive anomalies of Ba, K and Sr in borehole YT 1 (Fig. 5b), indicate that the concentrations of mobile elements may be modified by post-magmatic alteration. In a primitive mantle-normalized multi-

element diagram (Fig. 5b), they generally exhibit OIB-like trace element patterns with enrichment in some high field strength elements (HFSEs) (e.g., Th, U, Zr and Hf), whereas the samples from borehole TD 004 are characterized by slightly lower concentrations of HFSEs and LREEs relative to the samples from the other boreholes. The samples display large ion lithophile element (LILEs) enrichment, except for borehole TD 004 and ZJ 1 (Fig. 5b). Notably, most of the samples are characterized by no negative Nb-Ta anomalies and prominent K, P and Sr depletion. They also exhibit generally low Cr (33.8–99.0 ppm) and Ni (47.3–99.5 ppm) contents, consistent with evolved magmas as indicated by the low $Mg^{\#}$ values. Overall, the basalt samples from different boreholes in the SCB have REE and trace element patterns similar to both the average OIB composition and those of the basaltic outcropping sections within the ELIP.

4.2. Sr-Nd-Pb isotopes

Our new Sr, Nd and Pb isotope data of basaltic rocks from boreholes YT 1, ZG 1 and TD 004 in SCB are listed in Table 2 and plotted in Fig. 6. The $\varepsilon_{Nd}(t)$ and initial isotopic ratios have been recalculated at 260 Ma (Zhong et al., 2014). Since the Rb/Sr ratios may have been affected by secondary alteration, as indicated by the significant scatter in Rb/Sr of the ELIP and the studied basalts (Fig. 7a), this could affect the calculated age-corrected Sr isotope ratios. Thus, the Rb/Sr ratios of the least altered samples with low LOI (Rb/Sr = 0.03; LOI = 0.55; Li et al., 2017) was used to calculate the age-corrected Sr isotope ratios in all samples. The samples from borehole ZG 1 display a range of initial $^{87}Sr/^{86}Sr$ ratios between 0.706045 and 0.706801 and positive to slightly negative $\varepsilon_{Nd}(t)$ values ranging from −0.03 to 1.35. The borehole YT 1 samples have slightly more scattered initial $^{87}Sr/^{86}Sr$ ratios ranging from 0.706623 to 0.706945, and relatively low $\varepsilon_{Nd}(t)$ values from −0.01 to 0.33. In contrast, the borehole TD 004 samples show different slightly lower initial $^{87}Sr/^{86}Sr$ ratios of 0.705068–0.705244 and much higher $\varepsilon_{Nd}(t)$ values of 1.81–2.12 than borehole ZG 1 and YT 1. In the $\varepsilon_{Nd}(t)$ vs. ($^{87}Sr/^{86}Sr)_i$ diagram (Fig. 6a), the studied samples overlap with the fields of OIB and Emeishan flood basalts, in distinct contrast to the depleted mantle (DM). They also show relatively small ranges of age-corrected $^{206}Pb/^{204}Pb_{(t)}$ (ZG 1 = 18.167–18.636, YT 1 = 18.059–18.175 and TD 004 = 18.131–18.213), $^{207}Pb/^{204}Pb_{(t)}$ (ZG 1 = 15.581–15.608, YT 1 = 15.574–15.641 and TD 004 = 15.555–15.559)
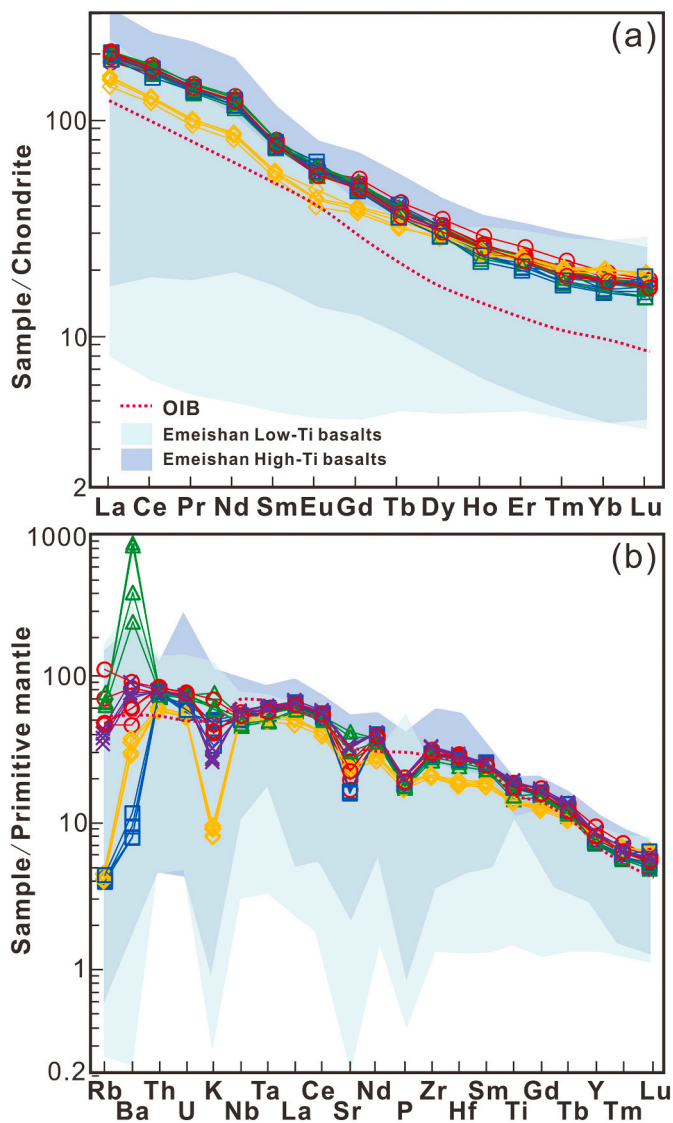
Fig. 5. (a) Chondrite-normalized REE patterns and (b) primitive mantle-normalized trace element patterns for the basaltic samples from boreholes in the Sichuan Basin. Chondrite and primitive mantle normalization values and OIB data (red dashed line) are from Sun and McDonough (1989). Data source for the Emeishan low-Ti and high-Ti basalts are the same as Fig. 4. Symbols as in Fig. 4. (For interpretation of the references to colour in this figure legend, the reader is referred to the web version of this article.)

and $^{208}Pb/^{204}Pb_{(t)}$ (ZG 1 = 38.537–38.984, YT 1 = 38.326–38.408 and TD 004 = 38.402–38.544) and fall within the OIB field in both the $^{207}Pb/^{204}Pb_{(t)}$ vs. $^{206}Pb/^{204}Pb_{(t)}$ and $^{208}Pb/^{204}Pb_{(t)}$ vs. $^{206}Pb/^{204}Pb_{(t)}$ diagrams (Fig. 6b and c). The samples overlap the DUPAL anomaly in Pb-isotopic space and have elevated $^{207}Pb/^{204}Pb_{(t)}$ and $^{208}Pb/^{204}Pb_{(t)}$ at a given $^{206}Pb/^{204}Pb_{(t)}$ relative to the Northern Hemisphere Reference Line (NHRL; Zindler and Hart, 1986; Fig. 6b and c).

5. Discussion

5.1. Spatial distribution of Permian basalts in the SCB

In recent decades, a large number of deep exploratory boreholes have been drilled in the SCB to gain understanding of hydrocarbon accumulation (Zou et al., 2014; Yang et al., 2021). These boreholes, which penetrated the deeply buried Permian basalt flows, revealed the presence of volcanic rocks, which lie outside the conventional areal

Table 2
Sr-Nd-Pb isotope results of Permian basalts from studied boreholes in SCB.

Sample no.	YT1-2	YT1-4	YT1-7	YT1-8	ZG1-1	ZG1-2	ZG1-3	ZG1-4	TD004-1	TD004-2	TD004-3	TD004-4
Rb (ppm)	49.01	49.92	46.90	57.55	48.01	31.57	76.36	32.36	3.00	2.96	2.64	2.75
Sr (ppm)	739	635	1017	933	436	372	585	502	508	547	533	542
Sm (ppm)	11.68	11.45	12.15	12.23	11.43	11.66	11.56	11.65	8.34	8.95	8.73	9.01
Nd (ppm)	55.50	53.68	57.91	59.25	53.60	55.40	56.46	56.83	38.15	40.78	40.18	41.31
$^{87}Rb/^{86}Sr$	0.19199274	0.227381	0.133463	0.178526	0.318667	0.245389	0.377825	0.186377	0.01708623	0.015645	0.014319	0.014664
$^{87}Sr/^{86}Sr$	0.707136	0.706982	0.707256	0.707304	0.707160	0.707082	0.707142	0.706404	0.705496	0.705603	0.705458	0.705427
2σ	0.000009	0.000007	0.000008	0.000009	0.000007	0.000007	0.000007	0.000009	0.000007	0.000006	0.000008	0.000007
$^{147}Sm/^{144}Nd$	0.1272	0.1289	0.1269	0.1247	0.1289	0.1273	0.1238	0.1240	0.1332	0.1346	0.1385	0.1390
$^{143}Nd/^{144}Nd$	0.512526	0.512540	0.512519	0.512527	0.512592	0.512573	0.512513	0.512518	0.512639	0.512638	0.512632	0.512635
2σ	0.000005	0.000006	0.000007	0.000007	0.000006	0.000007	0.000009	0.000006	0.000006	0.000006	0.000007	0.000005
$(^{87}Sr/^{86}Sr)_i$	0.706777	0.706623	0.706897	0.706945	0.706801	0.706723	0.706783	0.706045	0.705137	0.705244	0.705099	0.705068
$(^{143}Nd/^{144}Nd)_i$	0.512351	0.512363	0.512345	0.512356	0.512415	0.512398	0.512343	0.512348	0.512456	0.512453	0.512442	0.512444
$\varepsilon_{Nd}(t)$	0.11	0.33	−0.01	0.21	1.35	1.03	−0.03	0.06	2.12	2.05	1.81	1.85
U (ppm)	1.84	1.83	1.72	1.82	1.64	1.69	1.75	1.78	1.19	1.25	1.21	1.25
Th (ppm)	7.44	7.14	7.48	7.77	6.98	7.33	7.61	7.53	5.27	5.51	5.36	5.56
Pb (ppm)	24.6	15.5	6.48	6.43	6.85	17.7	8.05	8.31	5.69	4.75	5.05	5.12
$^{206}Pb/^{204}Pb$	18.3712	18.4757	18.7923	18.8122	18.9666	18.8901	18.7674	18.7350	18.7684	18.8280	18.8115	18.8092
2σ	0.0007	0.0006	0.0007	0.0007	0.0007	0.0006	0.0006	0.0007	0.0005	0.0007	0.0006	0.0006
$^{207}Pb/^{204}Pb$	15.6506	15.6463	15.6125	15.6125	15.6285	15.6207	15.6140	15.6096	15.5880	15.5909	15.5898	15.5901
2σ	0.0007	0.0005	0.0006	0.0007	0.0007	0.0006	0.0006	0.0006	0.0005	0.0006	0.0006	0.0006
$^{208}Pb/^{204}Pb$	38.6467	38.8010	39.3521	39.3713	39.4618	39.3425	39.3543	39.3189	39.3431	39.4052	39.4201	39.4083
2σ	0.0019	0.0015	0.0018	0.0017	0.0018	0.0017	0.0016	0.0016	0.0014	0.0016	0.0015	0.0014
$(^{206}Pb/^{204}Pb)_i$	18.175	18.166	18.088	18.059	18.325	18.636	18.191	18.167	18.213	18.131	18.175	18.158
$(^{207}Pb/^{204}Pb)_i$	15.641	15.632	15.576	15.574	15.596	15.608	15.584	15.581	15.559	15.555	15.557	15.557
$(^{208}Pb/^{204}Pb)_i$	38.389	38.408	38.354	38.326	38.577	38.984	38.538	38.537	38.544	38.402	38.502	38.469

Measured isotopic ratios of the studied samples were age-corrected to 260 Ma and the isotopic age corrected values are denoted with "i".
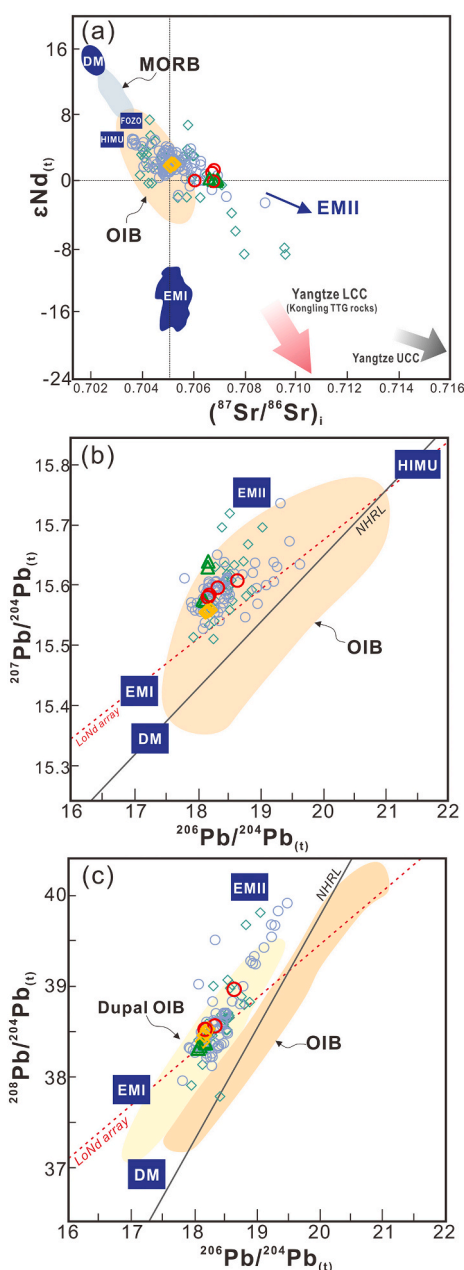
Fig. 6. Diagrams of (a) $\varepsilon_{Nd}(t)$ vs. $(^{87}Sr/^{86}Sr)_i$, (b) $^{207}Pb/^{204}Pb_{(t)}$ vs. $^{206}Pb/^{204}Pb_{(t)}$ and (c) $^{208}Pb/^{204}Pb_{(t)}$ vs. $^{206}Pb/^{204}Pb_{(t)}$ for basaltic rocks from boreholes in the Sichuan Basin. The field of OIB, Dupal OIB, DM, MORB, HIMU, EMI and EMII are after Hawkesworth et al. (1984), Hart (1988), Hamelin and Allègre (1985) and Weaver (1991). The NHRL and LoNd array are from Hart (1984). The Yangtze Block crustal compositions are taken from Chen and Jahn (1998), Gao et al. (1999), Ma et al. (2000) and Zhang et al. (2008). Data source for the Emeishan low-Ti and high-Ti basalts are the same as Fig. 4. Symbols as in Fig. 4.

extent of the ELIP, and thus provide us with sufficient information to draw a sketch map of Permian magmatic activity in the SCB (Ma et al., 2019; Xia et al., 2020). Based on drilling data collected from PetroChina and SINOPEC, the location and basalt thickness of boreholes in the SCB are illustrated in Fig. 1c. There are numerous boreholes (>100) that penetrated Permian basalts in the SCB and most of them are distributed in the southwestern (i.e. Emei and Yibin areas) and adjacent midwestern SCB (i.e. Chengdu and Santai areas). Notably, in addition to sporadic basalt outcrops in the Yanghe area (Li et al., 2017; Liu et al., 2020), Permian basaltic rocks have also been revealed in numerous

boreholes near the eastern boundary of the SCB (i.e. Liangping and Kaijiang areas), which was regarded as being located outside the known extent of the province. As shown by the stratigraphic correlation between volcanic sequences (Fig. 2), the studied basalts recovered from the SCB unconformably overlie the Middle Permian Maokou Formation or Kuhfeng Formation and are covered by the Late Permian Longtan Formation, indicating a contemporaneous relationship with the flood basalts in ELIP (He et al., 2007; Fan et al., 2008; Zhong et al., 2014; Huang et al., 2018). The comparable stratigraphical relations suggests that the Late Permian basalts in SCB may be a synchronous magmatic event with ELIP. The type, facies and thickness of volcanic rock sequences display significant variation from the southwestern part (200–350 m; large-scale overflow facies basaltic lavas) to the midwestern part (~200 m; eruptive facies pyroclastic rocks, basaltic lavas and diabase) and to the eastern part of the SCB (~60 m; basaltic lavas, minor diabase and dolerite dykes; Fig. 1c). Based on the lithology and thickness from available drilling data, the area and volume of concealed Permian SCB basaltic rocks, which was underestimated in previous studies, can be conservatively estimated to 6.5×10^4 km² and 2.4×10^3 km³, respectively.

5.2. Effects of alteration

As mentioned above, the studied samples have been variably altered, which makes it necessary to assess the relative mobility of elements to avoid pitfalls in the following discussion. The fluid-mobile elements (LILEs) and their ratios (e.g., Rb, K and Rb/Sr) display increased scatter for the higher LOI samples (Fig. 7a and b), which is a common feature of both high-Ti and low-Ti basalts in the ELIP (e.g., Xu et al., 2001, 2004, 2007; Zhang et al., 2006; Zhou et al., 2008; Kamenetsky et al., 2012; Li et al., 2016, 2017). Moreover, the mobile elements also show clear scatter when compared with immobile elements that are incompatible in early crystallizing phases of basaltic melts (e.g., Zr; Fig. 7d). In contrast, the strong linear correlations intersecting the origin between Zr and other immobile elements, such as La, irrespective of LOI (Fig. 7c), indicate that the magmas did not originate from distinct sources but by varying degrees of melting and variable extends of crystal fractionation (Zhang et al., 2006; Li et al., 2016). This suggests that in particular K and Rb concentrations have been altered by secondary processes. Some basalts from the borehole YT 1 and ZG 1 have elevated Rb, K and Sr concentrations, and the YT 1 also shows extremely high Ba concentrations, which could stem from zeolites and clay minerals in the vesicles (Fig. 5b), as has been documented in altered basalts elsewhere (e.g., Fleming et al., 1992; Søager and Holm, 2011; Millett et al., 2017). But for the basalts from boreholes TD 004 and ZJ 1, the mobile elements (e. g., Rb, Ba, K and Sr) are extremely depleted (e.g., K in TD 004 rocks and Ba in ZJ 1 rocks) resulting in Ba/Th ratios for the ZJ 1 rocks of 7–11 and K/Nb ratios of 53–61 for the TD 004 rocks. This is lower than even in the most extreme HIMU-type trace element patterns, e.g., the nephelinites of the Cape Verde islands (Barker et al., 2009; Holm et al., 2006). Furthermore, the trace element patterns of the ZJ 1 rocks are otherwise very similar to the YT 1, ZG 1 and JS 1 rocks indicating that they have not been generated from distinct mantle sources. Instead, the LILEs have probably been leached out of the samples from borehole TD 004 and ZJ 1 during secondary alteration. Therefore, we conclude that the mobile elements are unreliable and focus on the immobile elements in the following discussion.

5.3. Petrogenesis

5.3.1. Fractional crystallization and crustal contamination

The samples have low Mg# (36.9–43.2 ppm), Cr (34–99 ppm) and Ni (47–100 ppm) values, which are notably lower than those of primitive unfractionated magmas from the mantle (Mg# = 73–81, Cr > 1000 ppm, Ni > 400 ppm; Wilson, 1989), suggesting that the magmas underwent extensive fractional crystallization. Due to the quantitative limitation of
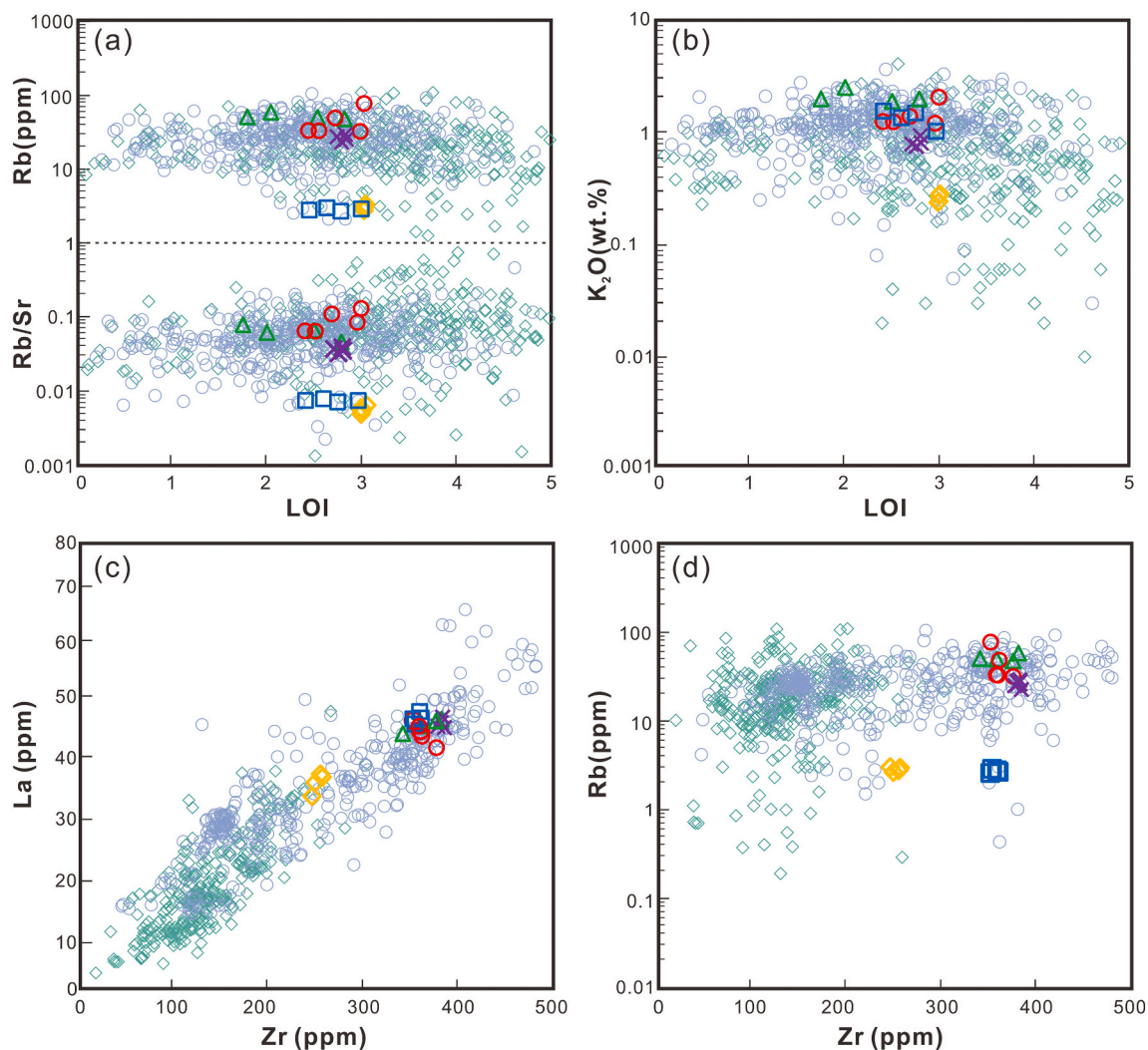
Fig. 7. Diagrams of (a) mobile elements Rb and Rb/Sr ratios vs. LOI, (b) K$_2$O vs. LOI, (c) incompatible elements La vs. incompatible elements Zr and (d) Rb vs. Zr. Data source for the Emeishan low-Ti and high-Ti basalts are the same as Fig. 4. Symbols as in Fig. 4.

core samples from borehole sampling, the fractionation trends in the Harker diagrams are not well constrained. However, we can still recognize positive correlations between Ni and Cr contents and CaO/Al$_2$O$_3$ ratios with MgO content in most of samples, which can be explained by fractionation of olivine and clinopyroxene respectively (Krienitz et al., 2006). The slightly negative anomalies of Eu (Eu/Eu* = 0.84–1.00) and depletion of Sr as shown in Fig. 5, suggest fractional crystallization of plagioclase.

The age-corrected Sr isotope ratios (i.e., (^{87}Sr/^{86}Sr)$_i$) of both the studied samples and high-Ti basalts in the ELIP display positive correlations with indicative trace element ratios for crustal contamination such as Th/Nb, La/Nb and Th/Yb and a negative correlation with Nb/U (Fig. 8). Moreover, the Sr isotope and trace element ratios extend to values outside the range of typical OIBs, indicating that the relatively high Sr-isotopic component may be derived from the crust and/or metasomatized subcontinental lithospheric mantle (SCLM), for example in the form of lamproitic/lamprophyric melts (McKenzie, 1989). One of the reasons why crustal contamination has been regarded as insignificant in the ELIP is because isotope and trace element ratios show poor correlations with indicators of magma fractionation, such as MgO, which could suggest that the geochemical variations were inherited from the mantle sources (Xiao et al., 2004; Fan et al., 2008; Li et al., 2016). The rare MgO-rich samples do show a significant variation, which would support this view (Fig. 9b). However, the majority of high-

Ti rocks have MgO < 7 wt% and have experienced extensive processing in magma chambers. In this group, the samples with elevated Th/Nb and Th/Yb and lower Nb/U also have some of the lowest MgO and highest SiO$_2$ (Fig. 9b–d), but the MgO contents generally show limited variation. In large magma chambers with recurrent recharge, evacuation, and fractional crystallization, the magmas evolve to increasingly high incompatible element contents while the MgO contents remain rather constant due to the repeated mafic recharge events (Lee et al., 2014; O'Hara, 1977). If concurrent crustal assimilation takes place in the magma chamber, the magmas will develop increasingly more crustal isotope and trace element ratios and higher SiO$_2$ with time without a large change in MgO. This was for example seen in LIP basalts from East Greenland in the North Atlantic Igneous Province (Hansen and Nielsen, 1999). It is a viable explanation for the large geochemical variations at almost constant MgO seen in the ELIP high-Ti basalts. However, distinguishing this process from magma evolution from a range of primitive magma compositions is very difficult and beyond the scope of this paper. But given the high flux of very hot magmas (up to >1500 °C; Yao et al., 2021) into the lower crust during the ELIP event, the most likely scenario is that crustal contamination was important and it should be considered seriously in future work.

As shown in Fig. 8, the correlations between (^{87}Sr/^{86}Sr)$_i$ and several trace element ratios can be modeled by assimilation and fractional crystallization (AFC) style contamination (DePaolo, 1981) similar to
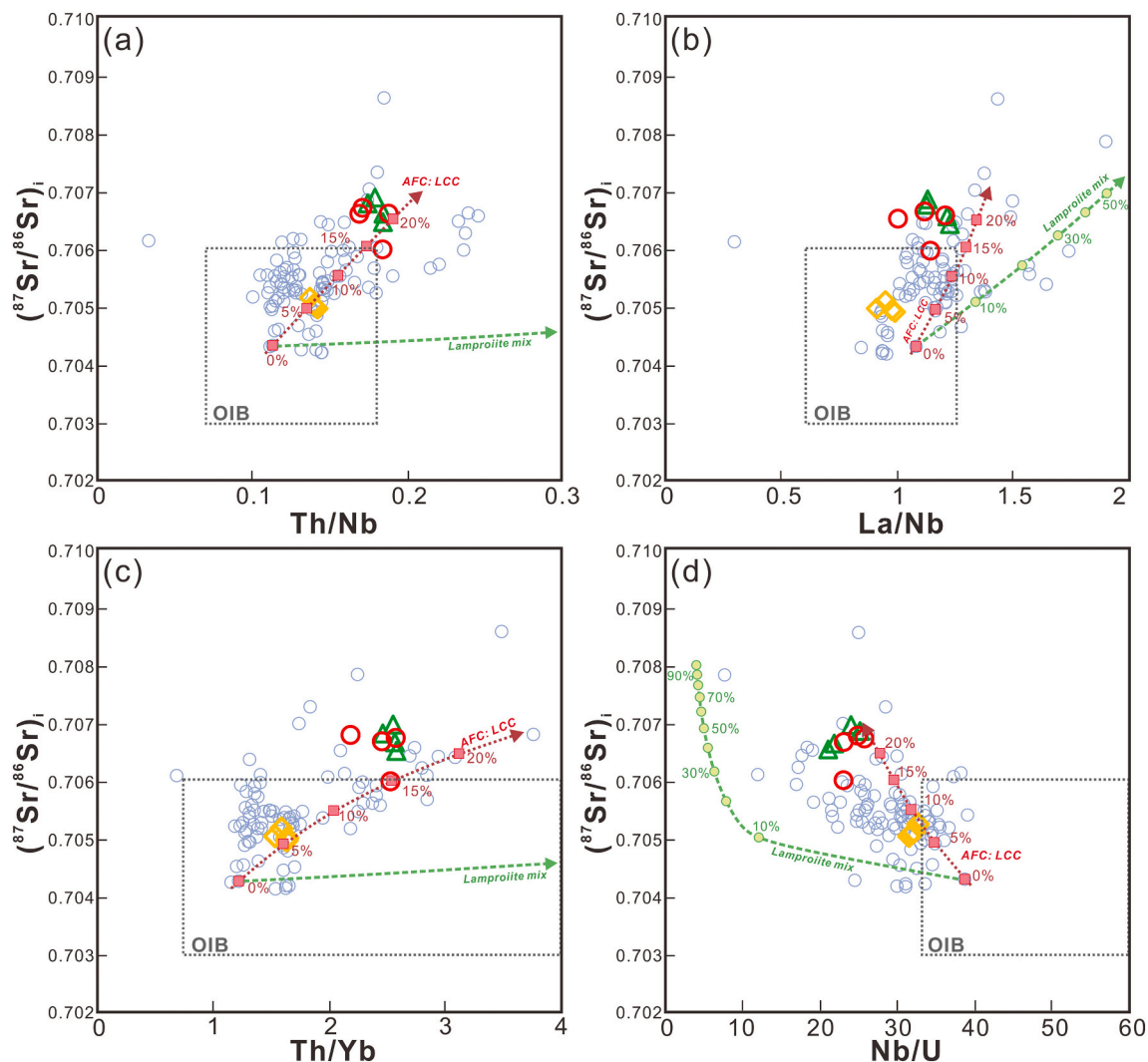
Fig. 8. Diagrams of (a) Th/Nb, (b) La/Nb, (c) Th/Yb and (d) Nb/U vs. (⁸⁷Sr/⁸⁶Sr)_i for the basaltic samples from boreholes in the Sichuan Basin and for the literature dataset of Emeishan high-Ti basalts. The range of OIB compositions are from Willbold and Stracke (2006) and Hofmann (2007) and reference therein. The pink dotted curves represent the percentage of assimilation of LCC melt (Qian and Hermann, 2013) based on the AFC modeling (DePaolo, 1981). The least contaminated basalt sample used as starting composition for the AFC model comes from Munteanu et al. (2017). The green dotted curves represent the mixing lines between a typical MgO-rich lamproite melt (Prelević et al., 2008) and the least contaminated basalt above. Data source for the Emeishan high-Ti basalts are the same as Fig. 4. Symbols as in Fig. 4. (For interpretation of the references to colour in this figure legend, the reader is referred to the web version of this article.)

what has been proposed for other LIPs (e.g., Heinonen et al., 2016, 2019). In this model, the ratio between the fractionating minerals olivine: plagioclase: clinopyroxene has been set to 0.1: 0.45: 0.45 according to the eutectic composition at 1 atm in the anorthite-diopside-forsterite system (Osborn and Tait, 1952). The r-value was set to 0.5 to obtain the necessary change in trace element and isotope compositions at the point when 55% melt remains. As starting composition, sample Gj2151B from Munteanu et al. (2017) with 8.5 wt% MgO was used, which means that the initial phase of crystallization dominated by olivine and clinopyroxene is not represented in this model. The partition coefficients used are from Mollo et al. (2013) (clinopyroxene), Sun et al. (2017) (plagioclase) and Jeffries et al. (1995) (olivine). Details of trace element and isotope compositions for the AFC modeling are listed in Table 3.

The observed correlations cannot be modeled by assimilation of upper crustal type material (here represented by the bulk average upper continental crust, UCC; Rudnick and Gao, 2003). UCC assimilation would cause too strong increase in Th relative to Nb and Ta and too little decrease in 1/Sr to explain the observed trends (Figs. 9a and 10b). Therefore, crustal contamination has hitherto been regarded as

insignificant in the ELIP high-Ti basalts (Wang et al., 2007; Lai et al., 2012; Li et al., 2017). However, assimilation of lower crustal melts (LCC melts), here represented by the experimental melt of average LCC (Rudnick and Gao, 2003) at 900 °C and 1.5 GPa (Qian and Hermann, 2013) (model lines shown in the diagrams), or average tonalitic–trondhjemitic–granodioritic (TTG) rocks can convincingly explain the observed trends (Figs. 8, 9 and 10). In a plot of (⁸⁷Sr/⁸⁶Sr)_i vs. 1/Sr (Fig. 9a), AFC and mixing models form straight lines. Therefore, if the negative trend formed by the ELIP high-Ti basalts and the TD 004 and YT 1 samples was produced by AFC, then the contaminant plots at the extension of the dominant sample trend at lower 1/Sr and higher Sr isotope values. This means that it cannot have had a higher Sr isotope value than ~0.710 because this is where the line intercepts the x-axis. The contaminating melt is, however, unlikely to have had a 1/Sr close to zero. Therefore, the ⁸⁷Sr/⁸⁶Sr of the contaminant was set to 0.709 in the model (Table 3). The Yangtze TTG basement rocks (Gao et al., 1999; Zhang, 2008) would be likely candidates as contaminants, but the Nd and Pb isotope values of these rocks are too unradiogenic to fit the model using the given element concentrations and ⁸⁷Sr/⁸⁶Sr of 0.709. Instead, the contaminant should have ¹⁴³Nd/¹⁴⁴Nd ~ 0.5118 and Pb-isotope
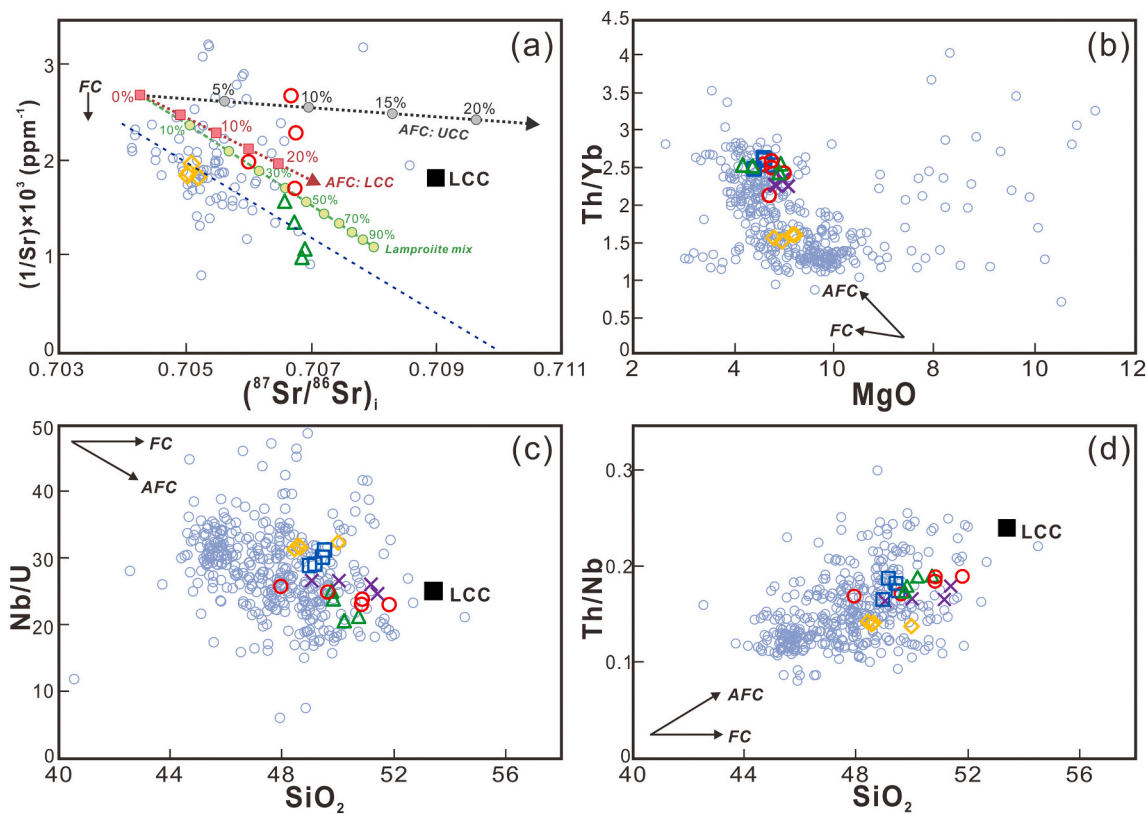
Fig. 9. Diagrams of (a) $(^{87}Sr/^{86}Sr)_i$ vs. $(1/Sr) \times 10^3$, (b) MgO vs. Th/Yb, (c) SiO$_2$ vs. Nb/U and (d) SiO$_2$ vs. Th/Nb for the basaltic samples from boreholes in the Sichuan Basin. The grey dotted curve shows the percentage of assimilation of bulk UCC $((^{87}Sr/^{86}Sr)_i = 0.720;$ Rudnick and Gao, 2003) using the AFC model. Parameters of the pink dotted curve of the AFC model and the green dotted mixing lines are same as Fig. 8. In (a), the blue dashed line highlights the negative trend of the main part of the data. Data for LCC are from Rudnick and Gao (2003) and reference therein. Data source for the Emeishan high-Ti basalts are the same as Fig. 4. Symbols as in Fig. 4. (For interpretation of the references to colour in this figure legend, the reader is referred to the web version of this article.)

Table 3
Trace element and isotope compositions used for the AFC modeling.

	$^{87}Sr/^{86}Sr$	Sr	Ta	U	Nb	La	Th	Yb	Reference
Starting magma	0.7043	371	1.17	0.49	19.2	20.6	2.2	1.80	Munteanu et al., 2017
LCC melt	0.7090*	538	0.84	0.90	11.1	32.5	5.7	0.20	Qian and Hermann, 2013
Average TTG	0.7090*	488	0.84§	0.94	5.2	23.1	5.2	0.73	Qian and Hermann, 2013
UCC	0.7200[#]	320	0.90	2.70	12.0	31.0	10.5	2.00	Rudnick and Gao, 2003

The Sr-isotope values of TTG and LCC melt marked by * are values chosen on the basis of data constraints and this value of UCC marked by [#] is a chosen value typical of upper continental crust. § value from Condie (2005).

ratios very similar to the basalts. Mafic lithologies such as gabbros in the lower crust could well have isotopic compositions like those indicated by the model, but it is, to our knowledge, not known if such compositions do exist in the Yangtze lower crust.

The model indicates up to more than 20% crust assimilation to explain the observed trends with the samples from boreholes in the western SCB (i.e., ZG 1, YT 1, ZJ 1 and JS 1) indicating higher amounts of crust assimilation than borehole TD 004 from the northeastern SCB. Such amounts seem unreasonably high, but we note that similar results were obtained for the Karoo basalts by simple AFC modeling (Luttinen et al., 1998; Luttinen and Furnes, 2000). It has later been shown that modeling by energy-constrained AFC (Bohrson and Spera, 2001; Spera and Bohrson, 2001) significantly reduces the required amount of crust assimilated (Heinonen et al., 2016, 2019). Therefore, a detailed modeling of both major and trace elements during fractionation and assimilation processes in, for example, the Magma Chamber Simulator software (Heinonen et al., 2019) should be undertaken to convincingly resolve the issue of the importance of crustal contamination.

An alternative possibility is that the observed correlations between

Sr isotopes and trace element ratios were formed by mixing between asthenospheric mantle melts and SCLM melts with higher $^{87}Sr/^{86}Sr$. An SCLM-type melt, which would increase Th/Nb, La/Nb, Th/Yb and $^{87}Sr/^{86}Sr$ and lower Nb/U could be a potassic melt, such as a lamproite melt, which owe their compositions to the addition of subducted sediments to their mantle source (Prelević et al., 2013). Both Himalayan and Mediterranean lamproites are extremely enriched in Th and U but have only moderate Sr-isotopes (~0.703–0.720) and most Himalayan lamproites cluster around $^{87}Sr/^{86}Sr \approx 0.708$ (Prelević et al., 2013). In Figs. 8, 9a and 10b, we have shown mixing lines between a typical MgO-rich lamproite melt (sample 03CX02 from Cancarix; Prelević et al., 2008), to which we have assigned a $^{87}Sr/^{86}Sr = 0.708$, and high-Ti sample Gj2151B from Munteanu et al. (2017). It is clear that the mixing lines do not reproduce the sample trends and we evaluate that lamproite melts are unlikely to contribute to the ELIP high-Ti basalts. The same is the case for the less potassic calc-alkaline lamprophyres from the North China Craton from Ma et al. (2014), which share the strong Th-U enrichment at moderate $^{87}Sr/^{86}Sr$ (~0.710) of the lamproites. Alkaline lamprophyres have similar or higher Nb/U as the ELIP high-Ti basalts
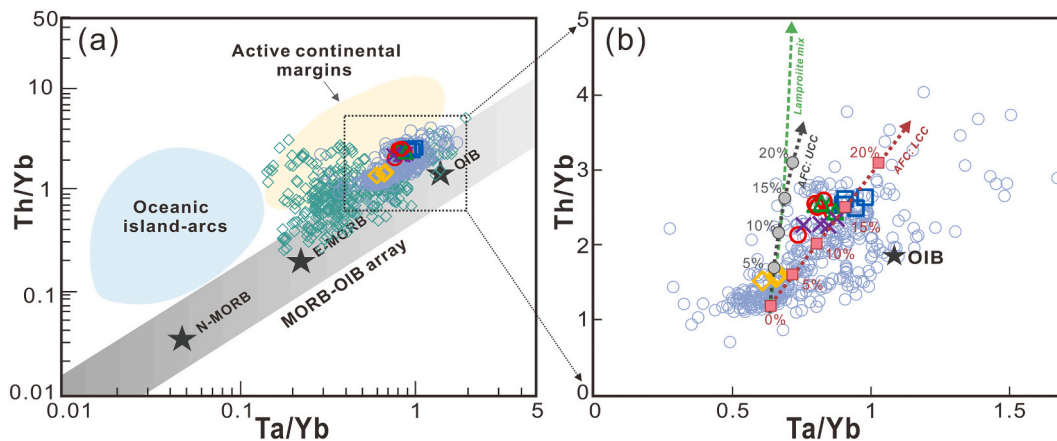
Fig. 10. Diagrams of Th/Yb vs. Ta/Yb (after Wilson, 1989 and Shellnutt, 2014) for the basaltic samples from boreholes in the Sichuan Basin. Data for N-MORB, E-MORB, OIB and PM are from Sun and McDonough (1989). (b) is a larger version of the area marked by the square in (a) to show the results of the contamination from LCC melts and bulk UCC by the AFC model and the mixing with lamproite melt. Parameters for the grey, pink, and green dotted curves as in Fig. 8. Data source for the Emeishan low-Ti and high-Ti basalts are the same as Fig. 4. Symbols as in Fig. 4. (For interpretation of the references to colour in this figure legend, the reader is referred to the web version of this article.)

and lower La/Nb (e.g., Batki et al., 2014; Bayat and Torabi, 2011; Orejana et al., 2008) and mixing with such melts would thus not lower the Nb/U and increase the La/Nb. Therefore, we favor the explanation that the trace element trends of the ELIP high-Ti basalts were generated by AFC processes in the crust.

5.3.2. Nature of mantle source

Primitive mantle-normalized trace element diagrams and chondrite-normalized REE diagrams (Fig. 5) suggest OIB-like magma sources for the basalts from both the western and northeastern SCB. As shown in Fig. 10, incompatible element ratios fall in the field of OIB and strongly resemble those of the Emeishan high-Ti basalts (e.g., Xu et al., 2001; Hanski et al., 2004; Fan et al., 2008; Shellnutt, 2014; Li et al., 2016, 2017). Although the samples may have been overprinted by crustal contamination, OIB-like isotopic characteristics of the studied basalts still can be identified in the plots of initial Sr-Nd-Pb isotopes (Fig. 6), indicating a genetic relation with the Emeishan flood basalts. Moreover, the crystallization temperature of clinopyroxenes, which can be used as an indicator for the thermal state of the mantle source for evolved magma (Putirka, 2008; Li et al., 2016), ranges from 1368 to 1432 °C for the Yanghe basalts (Li et al., 2017). Compared with the normal asthenospheric mantle (McKenzie and Bickle, 1988), the higher thermal state in the SCB is consistent with its location in the peripheral area of ELIP (Li et al., 2016, 2017). The basalts in the northeastern SCB (i.e. borehole TD 004 and Yanghe area; Li et al., 2017) are distinctly different from the basalts in the western SCB in that they have less steep REE patterns and lower abundances of incompatible trace elements. It is widely accepted that the ELIP is a typical plume-derived LIP and the basalts could be derived from heterogeneous mantle sources and with variable degrees of crustal contamination (Fan et al., 2008; Zhang et al., 2008; Lai et al., 2012; Shellnutt, 2014). As mentioned above, the similar incompatible element ratios and Sr-Nd-Pb isotopic values of most of the studied samples precludes the possibility that they originated from completely different mantle sources (Wang et al., 2004; Li et al., 2016).

The degree of partial mantle melting has been demonstrated by ample geochemical and geophysical studies to be highly dependent on the initial depth of melting (Niu and Batiza, 1991; Ellam, 1992; Langmuir et al., 1992; DePaolo and Daley, 2000; Zhang et al., 2019). Distinct REE patterns as well as ratios (e.g., Sm/Yb, Dy/Yb and Tb/Yb) enable an estimation of the degree of partial melting and also degree of magma source enrichment (Aldanmaz et al., 2000; Hellebrand et al., 2002). Compared with the borehole TD 004 basalts (Dy/Yb = 2.16–2.20), the samples from boreholes in the western SCB have relatively high Dy/Yb

ratios (2.53–2.87) suggesting more garnet in the partial melting residue and thus deeper mantle melting (Duggen et al., 2005; Jiang et al., 2009). Moreover, the western SCB data, similar to the high-Ti basalts in the eastern ELIP, lie closer to a melting trajectory with higher garnet contents (garnet/spinel>1), whereas the northeastern basalts plot at the trajectory for the source with equal quantities of spinel and garnet (i.e., spinel and garnet transition; Aldanmaz et al., 2000; Wang et al., 2007; Qi and Zhou, 2008; Fig. 11a). On the basis of $(Tb/Yb)_p$ (normalized to primitive mantle; Sun and McDonough, 1989) vs. $(Yb/Sm)_p$, the data in the western SCB are consistent with more residual garnet (~70%) relative to spinel in the source compared with the northeastern samples (~50%; Fig. 11b). Based on the assumptions of model calculations, the degrees of partial melting were probably ~5% and less than ~3% for the parental magmas of the basalts from boreholes in the northeastern and western SCB, respectively (Fig. 11).

5.4. Insight into the origin of Emeishan basalts in the SCB and environmental implications

The Emeishan basalts are generally considered as the products of melting of a mantle plume with possible interactions between the plume melts and lithospheric sources such as crustal materials and SCLM components (e.g., Xu et al., 2001; Xiao et al., 2004; Fan et al., 2008). Interestingly, in contrast to the basalts in the western SCB, melts that generated the northeastern SCB basalts seem to have formed at a shallower depth, which is inconsistent with the generally accepted Emeishan model (e.g., Xu et al., 2001). Thus, what kind of geodynamic mechanism is responsible for the Emeishan basalts in the SCB? The analysis of the Late Paleozoic tectonic evolution in the Upper Yangtze block may enlighten this question. Paleozoic plate reconstructions show that the Upper Yangtze region in the South China Block was located in the eastern Paleotethyan realm near the equator (~2.4°N; Cocks and Torsvik, 2013; Jerram et al., 2016; Huang et al., 2021; Fig. 1a), and was separated from the North China Block and the Simao-Indochina Block by the Mianlue Ocean in the north and the Jinshajiang-Ailaoshan Ocean in the south (Cai and Zhang, 2009; Metcalfe, 2013; Zhao et al., 2018). It is worth noting that, in addition to the well-known Emeishan taphrogenesis in the western Upper Yangtze block, the northern part of this block (i.e., the northern SCB) was a passive margin at 300–250 Ma, due to northward subduction of the Mianlue oceanic plate towards the North China Block (Zhang et al., 1996, 2003, 2013; Li et al., 2019; Liu et al., 2021). This led to an extensional tectonic setting in the SCB during Middle-Late Permian. As mentioned earlier, there is a good correlation
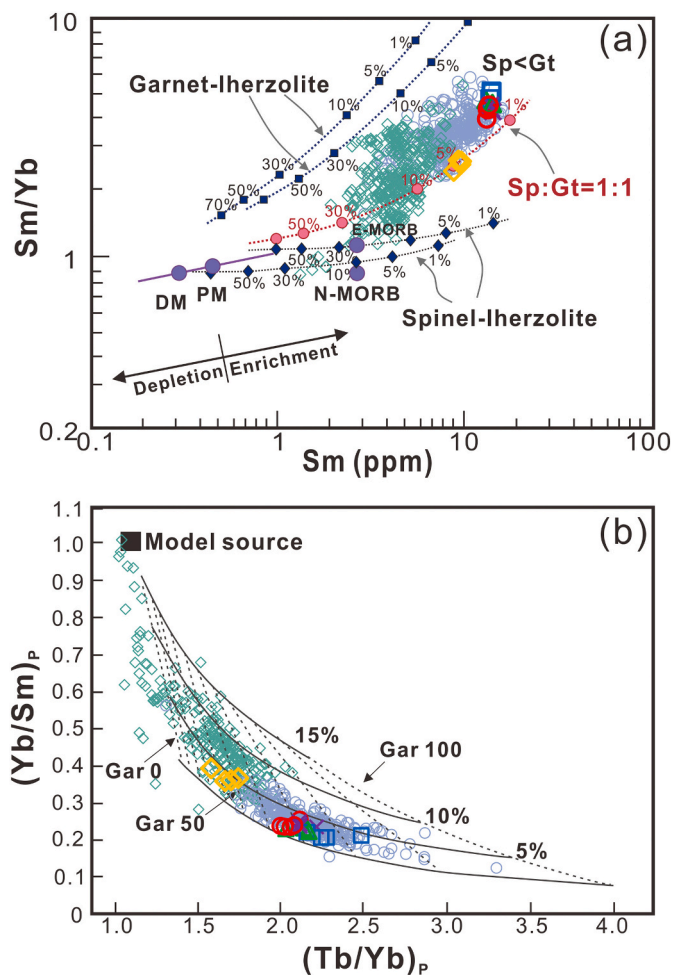
Fig. 11. Diagrams of (a) Sm/Yb vs. Sm and (b) $(Yb/Sm)_P$ vs. $(Tb/Yb)_P$ showing mantle melting curves relevant for the basaltic samples from boreholes in the Sichuan Basin, after Aldanmaz et al. (2000), Zhang et al. (2006) and references therein. Melt curves in (a) are drawn for spinel lherzolite and garnet lherzolite; Numbers on the melt curves refer to percentages of melting in a given mantle source as Aldanmaz et al. (2000). The grid in (b) indicates the range of model melt compositions produced by aggregated fractional melting of peridotite; the solid lines indicate constant melt fraction. The dotted curves show the percentage of melt contribution from garnet-facies mantle vs. spinel-facies mantle. Mineral/matrix partition coefficients and DM are from McKenzie and O'Nions (1991, 1995). PM, N-MORB and E-MORB compositions are from Sun and McDonough (1989) and Workman and Hart (2005). Data sources for the Emeishan low-Ti and high-Ti basalts are the same as Fig. 4. Symbols as in Fig. 4.

between the distribution of the Late Permian basalts and the intersection of the NE-trending Huayingshan basement fault and the NW-trending faulting system in the eastern SCB (Fig. 1c). Finite element simulation and stress-field data has confirmed that the extension in the fault systems can result in the large-scale crustal density contrast as well as the sudden change of transient pressure, providing a decompression mechanism to generate melts in areas where mantle rocks are already close to their solidus (Connor et al., 2000; Geoffroy et al., 2015). Thus, we propose a possible integrated tectonic model to explain the spatio-temporal scenario and geochemical variation of the Emeishan basalts in the SCB (Fig. 12).

In the Middle-Late Permian, the impingement of the Emeishan mantle plume on the lithosphere caused a regional-scale updoming in the southwestern Upper Yangtze block, leading to decompression melting of mantle and emplacement of thick piles of flood basalts, including the basalts in the western SCB (Fig. 12a). Meanwhile, significant regional extension caused by both the Emeishan plume and the

Mianlue Ocean subduction had affected the lithosphere of the SCB, resulting in the reactivation of pre-existing basement faults in this basin. Magmas were generated from the periphery of the plume head below these weakness zones of thinned lithosphere by decompression melting and emplaced in discrete areas (i.e. borehole TD 004 and Yanghe area) separate from the large-scale flood basalts in the ELIP (Fig. 12b).

The emplacement of voluminous LIP magmas, as widely confirmed in the 251 Ma Siberian Traps, 201 Ma Central Atlantic Magmatic Province and 66 Ma Deccan Traps, could trigger massive releases of particulate and gasses (e.g., SO_2, CO_2 and halogens), leading to the environmental catastrophes and even mass extinction events throughout Earths history (Ganino and Arndt, 2009; Svensen et al., 2009; Sobolev et al., 2011; Ernst and Youbi, 2017; (Elkins-Tanton et al., 2020) and reference therein). Recent studies suggested that the carbon and sulfur degassing from the Emeishan mantle plume directly contributed to the end-Guadalupian abrupt climatic change and mass extinction event (Ganino and Arndt, 2009; Zhu et al., 2021a, 2021b). The identification of widespread Emeishan basalts in the SCB broadens the previous understanding of areal extent and volume of the ELIP. The radius of the ELIP is ~100 km larger, i.e., 700–800 km measured directly, than the previous estimates (e.g., Li et al., 2017). Combined with previous analyses of Emeishan volcanic rocks (including the northern Vietnam volcanic rocks; Shellnutt et al., 2020), we infer that the spatial extent of the ELIP might be larger than the 1×10^6 km^2 as proposed by Li et al. (2017). Moreover, the same origin of basalts in the SCB as the ELIP may be the most reasonable explanation for the abrupt elevation of the thermal state of the basin sedimentary rocks in the SCB during the Middle-Late Permian (Zhu et al., 2016, Zhu et al., 2018a, 2018b; Jiang et al., 2018; Xu et al., 2018). Thus, not only the mantle-derived magmas degassed, the extensive heating of multiple dolomites, evaporites and organic-rich shales of ancient marine sequences in the SCB may also have released large quantities of greenhouse and toxic gases (Ganino and Arndt, 2009; Svensen et al., 2009; Sobolev et al., 2011; Jones et al., 2016). So even though the stature of the ELIP is not as big as the Siberian Traps, it still can be speculated that the extension of the ELIP in the SCB led to the release of large quantities of carbon and sulfur to the atmosphere. Accordingly, our study may further strengthen the possible link between the Emeishan volcanism and Middle-Late Permian climate change as well as the end-Guadalupian mass extinction and may shed some light on the study of the interaction between plume melts and sedimentary basins.

6. Conclusions

(1) The basaltic flows interlayered with Middle-Late Permian sedimentary rocks in the SCB can be geochemically subdivided into two groups. The western SCB group had a deep source predominantly in the garnet stability field, whereas the northeastern SCB group came from a shallower magma source in the spinel-garnet transition zone. All these basalts were derived from an OIB-like mantle plume source and were possibly overprinted by LCC contamination.

(2) The Permian basalts in the SCB were likely generated in response to plume-lithosphere interaction in which the weakness zones of the lithosphere may have had a significant impact on the distribution of these basalts, indicating that ELIP may extend over a substantially broader region than previously estimated.

(3) Such large-scale emplacement of mafic magmas from the Emeishan mantle plume in a petroliferous basin was a possible contributor to climate changes as well as the biological crisis at the end-Guadalupian.

Declaration of Competing Interest

The authors declare that they have no known competing financial interests or personal relationships that could have appeared to influence
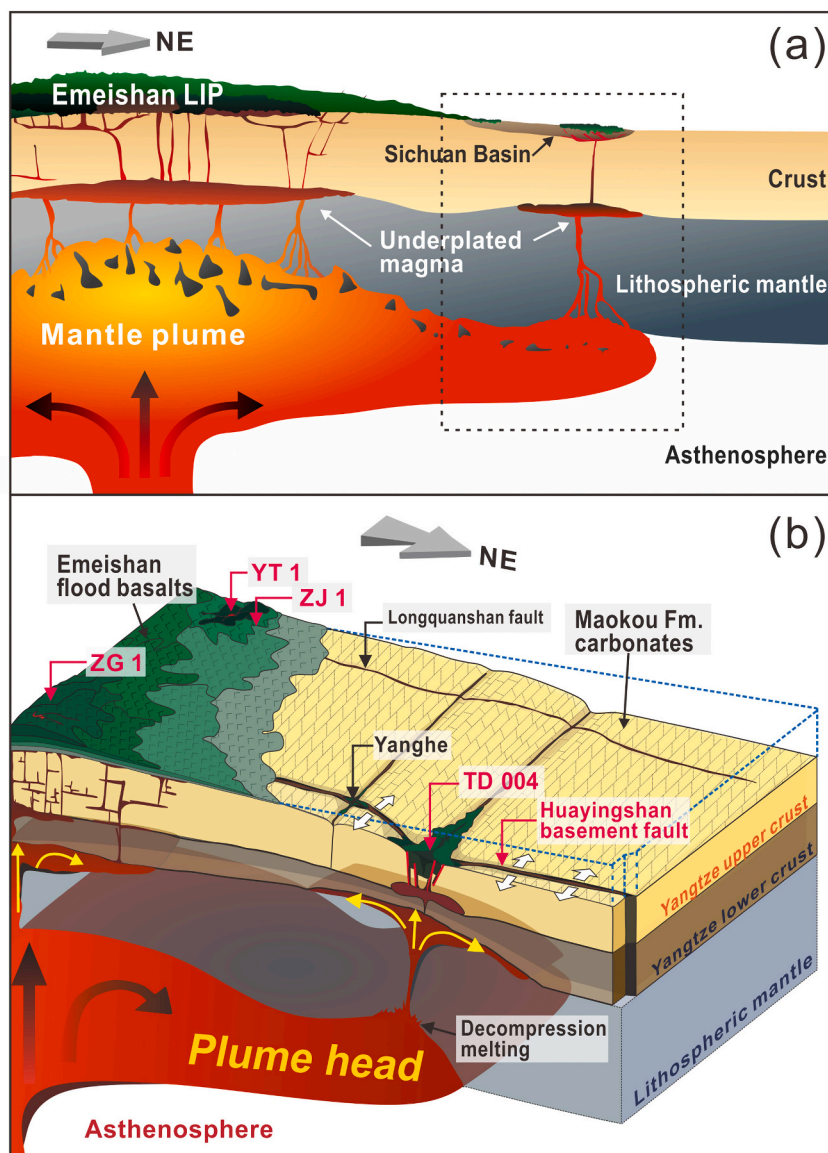
Fig. 12. (a) Cartoon showing the interaction between ascending Emeishan mantle plume magmas with the lithospheric mantle and crust, resulting in the large-scale emplacement of the Emeishan flood basalts. (b) Schematic model for genesis of the Permian basalts in the Sichuan Basin (see text for discussion).

the work reported in this paper.

References

Aldanmaz, E., Pearce, J.A., Thirlwall, M.F., Mitchell, J.G., 2000. Petrogenetic evolution of late Cenozoic, post-collision volcanismin western Anatolia, Turkey. J. Volcanol. Geotherm. Res. 102, 67–95.

Ali, J.R., Fitton, J.G., Herzberg, C., 2010. Emeishan large igneous province (SW China) and the mantle-plume up-doming hypothesis. J. Geol. Soc. 167, 953–959.

Baker, J., Peate, D., Waight, T., Meyzen, C., 2004. Pb isotopic analysis of standards and samples using a 207Pb-204Pb double spike and thallium to correct for mass bias with a double-focusing MC-ICP-MS. Chem. Geol. 211 (3–4), 275–303.

Barker, A.K., Holm, P.M., Peate, D.W., Baker, J.A., 2009. Geochemical stratigraphy of submarine lavas (3–5 Ma) from the Flamengos Valley, Santiago, Southern Cape Verde Islands. J. Petrol. 50 (1), 169–193.

Batki, A., Pál-Molnár, E., Dobosi, G., Skelton, A., 2014. Petrogenetic significance of ocellar camptonite dykes in the Ditrău Alkaline Massif, Romania. Lithos 200-201, 181–196.

Bayat, F., Torabi, G., 2011. Alkaline lamprophyric province of Central Iran. Island Arc 20, 386–400.

Bohrson, W.A., Spera, F.J., 2001. Energy-constrained open-system magmatic processes II: application of energy-constrained assimilation-fractional crystallization (EC-AFC) model to magmatic systems. J. Petrol. 42, 1019–1041.

Bryan, S.E., Ernst, R.E., 2008. Revised definition of Large Igneous Provinces (LIPs). Earth Sci. Rev. 86, 175–202.

Bryan, S.E., Ferrari, L., 2013. Large igneous provinces and silicic large igneous provinces: Progress in our understanding over the last 25 years. Geol. Soc. Am. Bull. 125 (7–8), 1053–1078.

Cai, J.X., Zhang, K.J., 2009. A new model for the Indochina and south china collision during the late Permian to the middle Triassic. Tectonophysics 467 (1–4), 35–43.

Campbell, I.H., 2005. Large igneous provinces and the mantle plume hypothesis. Elements 1 (5), 265–269.

Campbell, I.H., Griffiths, R.W., 1990. Implications of mantle plume structure for the evolution of flood Basalts. Earth Planet. Sci. Lett. 99, 79–93.

Charvet, J., 2013. The neoproterozoic-early paleozoic tectonic evolution of the south china block: an overview. J. Asian Earth Sci. 74 (25), 198–209.

Chen, J.F., Jahn, B.M., 1998. Crustal evolution of southeastern China: Nd and Sr isotopic evidence. Tectonophysics 284, 101–133.

Chen, J., Xu, Y.G., 2019. Establishing the link between Permian volcanism and biodiversity changes: Insights from geochemical proxies. Gondwana Res. 75, 68–96.

Chen, Y., Xu, Y.G., Xu, T., Si, S.K., Liang, X.F., Tian, X.B., Deng, Y.F., Chen, L., Wang, P., Xu, Y.H., Lan, H.Q., Xiao, F.H., Li, W., Zhang, X., Yuan, X.H., Badal, J., Teng, J.W., 2015. Magmatic underplating and crustal growth in the Emeishan Large Igneous Province, SW China, revealed by a passive seismic experiment. Earth Planet. Sci. Lett. 432, 103–114.

Chen, Y., Wang, Z.H., Guo, X., Deng, Y.F., Xu, T., Liang, X.F., Tian, X.B., Wi, J., Chen, L., Zhang, X., Tang, G.B., Xu, Y.G., 2017. Geophysical signature of the ancient mantle plume activities: a case study of the Emeishan large igneous province. Bull. Mineral. Petrol. Geochem. 36 (3), 394–403 (in Chinese with English abstract).

Chung, S.L., Jahn, B.M., 1995. Plume-lithosphere interaction in generation of the Emeishan flood basalts at the Permian-Triassic boundary. Geology 23, 889–892.

Chung, S.L., Jahn, B.M., Wu, G.Y., Lo, C.H., Cong, B., 1998. The Emeishan flood basalt in SW China: a mantle plume initiation model and its connection with continental breakup and mass extinction at the Permian-Triassic boundary. In: Flower, M.F.J., Chung, S.L., Lo, C.H., Lee, T.Y. (Eds.), Mantle Dynamics and Plate Tectonics in East Asia, AGU Geodynamics Series, 27, pp. 47–58.

Cocks, L.R.M., Torsvik, T.H., 2013. The dynamic evolution of the Palaeozoic geography of eastern Asia. Earth Sci. Rev. 117, 40–79.

Condie, K.C., 2005. TTGs and adakites: are they both slab melts? Lithos 80 (1–4), 33–44.

Connor, C.B., Stamatakos, J.A., Ferrill, D.A., Hill, B.E., Ofoegbu, G.I., Conway, F.M., Sagar, B., Trapp, J., 2000. Geologic factors controlling patterns of small-volume basaltic volcanism: application to a volcanic hazards assessment at Yucca Mountain, Nevada. J. Geophys. Res. Solid Earth 105 (B1), 417–432.

Dai, J., Zou, C., Liao, S., Dong, D., Ni, Y., Huang, J., Wu, W., Gong, D., Huang, S., Hu, G., 2014. Geochemistry of the extremely high thermal maturity Longmaxi shale gas, southern Sichuan Basin. Org. Geochem. 74, 3–12.

Deng, X.S., Yang, J.H., Cawood, P.A., Wang, X.C., Du, Y.S., Huang, Y., Lu, S.F., He, B., 2020. Detrital record of late-stage silicic volcanism in the Emeishan large igneous province. Gondwana Res. 79, 197–208.

DePaolo, D.J., 1981. Trace element and isotopic effects of combined wall rock assimilation and fractional crystallization. Earth Planet. Sci. Lett. 53 (2), 189–202.

DePaolo, D.J., Daley, E.E., 2000. Neodymium isotopes in basalts of the southwest basin and range and lithospheric thinning during continental extension. Chem. Geol. 169, 157–185.

Duggen, S., Hoernle, K., van den Bogaard, P., Garbe-Schönberg, D., 2005. Post-collisional transition from subduction to intraplate-type magmatism in the westernmost Mediterranean: evidence for continental-edge delamination of subcontinental lithosphere. J. Petrol. 46, 1155–1201.

Elkins-Tanton, L.T., Grasby, S.E., Black, B.A., Veselovskiy, R.V., Ardakani, O.H., Goodarzi, F., 2020. Field evidence for coal combustion links the 252 Ma Siberian Traps with global carbon disruption. Geology 48 (10), 986–991.

Ellam, R.M., 1992. Lithospheric thickness as a control on basalt geochemistry. Geology 20, 153–156.

Ernst, R.E., 2014. Large Igneous Provinces. Cambridge University Press, Oxford, pp. 1–641.

Ernst, R.E., Youbi, N., 2017. How Large Igneous Provinces affect global climate, sometimes cause mass extinctions, and represent natural markers in the geological record. Palaeogeogr. Palaeoclimatol. Palaeoecol. 478, 30–52.

Ernst, R.E., Buchan, K.L., Campbell, I.H., 2005. Frontiers in large igneous province research. Lithos 79, 271–297.

Fan, W.M., Zhang, C.H., Wang, Y.J., Guo, F., Peng, T.P., 2008. Geochronology and geochemistry of Permian basalts in western Guangxi Province, Southwest China: evidence for plume-lithosphere interaction. Lithos 102, 218–236.

Feng, K., Xu, S.L., Chen, A.Q., Ogg, J., Hou, M.C., Lin, L.B., Chen, H.D., 2021. Middle permian dolomites of the sw Sichuan basin and the role of the Emeishan large igneous province in their origin. Mar. Pet. Geol. 128, 104981.

Fleming, T.H., Elliot, D.H., Jones, L.M., Bowman, J.R., Siders, M.A., 1992. Chemical and isotopic variations in an ironrich lava flow from the Kirkpatrick Basalt, North Victoria Land, Antarctica: implications for low-temperature alteration. Contrib. Mineral. Petrol. 111, 440–457.

Ganino, C., Arndt, N.T., 2009. Climate changes caused by degassing of sediments during the emplacement of large igneous provinces. Geology 37, 323–326.

Gao, S., Ling, W., Qiu, Y., Lian, Z., Hartmann, G., Simon, K., 1999. Contrasting geochemical and Sm-Nd isotopic compositions of Archean metasediments from the Kongling high-grade terrain of the Yangtze craton: evidence for cratonic evolution and redistribution of REE during crustal anatexis. Geochim. Cosmochim. Acta 63 (13–14), 2071–2088.

Geoffroy, L., Burov, E.B., Werner, P., 2015. Volcanic passive margins: another way to break up continents. Sci. Rep. 5, 14828.

Han, W., Luo, J.H., Fan, J.L., Cao, Y.Z., Zhang, Y.J., 2009. Late Permian Diabase in Luodian, Southeastern Guizhou and its tectonic significance. Geol. Rev. 55 (6), 795–803 (in Chinese with English abstract).

Hansen, H., Nielsen, T.F.D., 1999. Crustal contamination in Palaeogene East Greenland flood basalts: plumbing system evolution during continental rifting. Chem. Geol. 157, 89–118.

Hanski, E., Walker, R.J., Huhma, H., Polyakov, G.V., Balykin, P.A., Hoa, T.T., Phuong, N. T., 2004. Origin of the Permian-Triassic komatiites, northwestern Vietnam. Contrib. Mineral. Petrol. 147, 453–469.

Hart, S.R., 1984. The Dupal anomaly: a large-scale isotopic anomaly in the southern hemisphere. Nature 309, 753–756.

Hart, S.R., 1988. Heterogeneous mantle domains: signature, genesis and mixing chronologies. Earth Planet. Sci. Lett. 90, 273–296.

Hawkesworth, C.J., Rogers, N.W., van Calsteren, P.W.C., Menzies, M.A., 1984. Mantle enrichment processes. Nature 311 (27), 331–335.

He, L.J., 2020. Thermal evolution of the upper yangtze craton: secular cooling and short-lived thermal perturbations. Phys. Earth Planet. Inter. 301, 106458.

He, B., Xu, Y.G., Xiao, L., Chung, S., Wang, Y.M., 2003. Sedimentary evidence for a rapid, kilometer-scale crustal doming prior to the eruption of the Emeishan flood basalts. Earth Planet. Sci. Lett. 213, 391–405.

He, B., Xu, Y.G., Huang, X.L., Luo, Z.Y., Shi, Y.R., Yang, O.J., Yu, S.Y., 2007. Age and duration of the Emeishan flood volcanism, SW China: geochemistry and SHRIMP zircon U-Pb dating of silicic ignimbrites, post-volcanic Xuanwei formation and clay tuff at the Chaotian section. Earth Planet. Sci. Lett. 255, 306–323.

He, B., Xu, Y.G., Zhong, Y.T., Guan, J.P., 2010. The Guadalupian-Lopingian boundary mudstones at Chaotian (SW China) are clastic rocks rather than acidic tuffs: implication for a temporal coincidence between the end-Guadalupian mass extinction and the Emeishan volcanism. Lithos 119, 10–19.

Heinonen, J.S., Luttinen, A.V., Bohrson, W.A., 2016. Enriched continental flood basalts from depleted mantle melts: modeling the lithospheric contamination of Karoo lavas from Antarctica. Contrib. Mineral. Petrol. 171 (1), 1–22.

Heinonen, J.S., Luttinen, A.V., Spera, F.J., Bohrson, W.A., 2019. Deep open storage and shallow closed transport system for a continental flood basalt sequence revealed with Magma Chamber Simulator. Contrib. Mineral. Petrol. 174 (11), 1–18.

Hellebrand, E., Snow, J.E., Hoppe, P., Hofmann, A.W., 2002. Garnet-field melting and late-stage refertilization in 'residual' abyssal peridotites from the Central Indian Ridge. J. Petrol. 43 (12), 2305–2338.

Hofmann, A.W., 2007. Sampling mantle heterogeneity through oceanic basalts: isotopes and trace elements. In: Holland, H.D., Turekian, K.K. (Eds.), Treatise on Geochemistry. Pergamon, Oxford, pp. 1–44.

Holm, P.M., Wilson, J.R., Christensen, B.P., Hansen, L., Hansen, S.L., Hein, K.M., Mortensen, A.K., Pedersen, R., Plesner, S., Runge, M.K., 2006. Sampling the Cape Verde mantle plume: evolution of melt compositions on Santo Antão, Cape Verde Islands. J. Petrol. 47 (1), 145–189.

Hou, T., Zhang, Z.C., Kusky, T., Du, Y.S., Liu, J.L., Zhao, Z.D., 2011. A reappraisal of the high-Ti and low-Ti classification of basalts and petrogenetic linkage between basalts and mafic–ultramafic intrusions in the Emeishan Large Igneous Province, SW China. Ore Geol. Rev. 41, 133–143.

Huang, H., Cawood, P.A., Hou, M.C., Yang, J.H., Ni, S.J., Du, Y.S., Yan, Z.K., Wang, J., 2016. Silicic ash beds bracket Emeishan large igneous province to < 1 my. At ~260 Ma. Lithos 264, 17–27.

Huang, H., Cawood, P.A., Hou, M.C., Ni, S.J., Yang, J.H., Du, Y.S., Wen, H.G., 2018. Provenance of Late Permian volcanic ash beds in South China: implications for the age of Emeishan volcanism and its linkage to climate cooling. Lithos 4, 293–306.

Huang, H.Y., He, D.F., Li, Y.Q., Li, D., Zhang, Y.Y., Chen, J.J., 2021. Late Permian tectono-sedimentary setting and basin evolution in the Upper Yangtze region, South China: implications for the formation mechanism of intra-platform depressions. J. Asian Earth Sci. https://doi.org/10.1016/j.jseaes.2020.104599.

Ivanov, A.V., 2007. Evaluation of different models for the origin of the Siberian Traps. Spec. Pap. Geol. Soc. Am. 430, 669.

Jeffries, T.E., Perkins, W.T., Pearce, N.J.G., 1995. Measurements of trace elements in basalts and their phenocrysts by laser probe microanalysis inductively coupled plasma mass spectrometry (LPMA-ICP-MS). Chem. Geol. 121, 131–144.

Jerram, D.A., Widdowson, M., Wignall, P.B., Sun, Y.D., Lai, X.L., Bond, D., Torsvik, T.H., 2016. Submarine palaeoenvironments during Emeishan flood basalt volcanism, SW China: implications for plume-lithosphere interaction during the Capitanian, Middle Permian ('end Guadalupian') extinction event. Palaeogeogr. Palaeoclimatol. Palaeoecol. 441 (1), 65–73.

Jiang, Y.H., Jiang, S.Y., Dai, B.Z., Liao, S.Y., Zhao, K.D., Ling, H.F., 2009. Middle to Late Jurassic felsic and mafic magmatism in southern Hunan province, southeast China: implications for a continental arc to rifting. Lithos 107, 185–204.

Jiang, Q., Qiu, N.S., Zhu, C.Q., 2018. Heat flow study of the Emeishan large igneous province region: implications for the geodynamics of the Emeishan mantle plume. Tectonophysics 724, 11–27.

Jones, M.T., Jerram, D.A., Svensen, H.H., Grove, C., 2016. The effects of large igneous provinces on the global carbon and sulphur cycles. Palaeogeogr. Palaeoclimatol. Palaeoecol. 441, 4–21.

Kamenetsky, V.S., Chung, S.L., Kamenetsky, M.B., Kuzmin, D.V., 2012. Picrites from the Emeishan Large Igneous Province, SW China: a compositional continuum in primitive magmas and their respective mantle sources. J. Petrol. 53, 2095–2113.

Krienitz, M.S., Haase, K.M., Mezger, K., Eckardt, V., Shaikh-Mashail, M.A., 2006. Magma genesis and crustal contamination of continental intraplate lavas in northwestern Syria. Contrib. Mineral. Petrol. 151, 698–716.

Lai, S.C., Qin, J.F., Li, Y.F., Li, S.Z., Santosh, M., 2012. Permian high Ti/Y basalts from the eastern part of the Emeishan Large Igneous Province, southwestern China: petrogenesis and tectonic implications. J. Asian Earth Sci. 47, 216–230.

Langmuir, C.H., Klein, E.M., Plank, T., 1992. Petrological systematics of mid-ocean ridge basalts: constraints on melt generation beneath ocean ridges. In: Morgan, J.P., Blackman, D.K., Sinton, J.M. (Eds.), Mantle Flow and Melt Generation at Mid-Ocean Ridges. Geophysical Monograph Serial of AGU, Washington, D.C., pp. 183–280.

Lee, C.T.A., Lee, T.C., Wu, C.T., 2014. Modeling the compositional evolution of recharging, evacuating, and fractionating (REFC) magma chambers: implications for differentiation of arc magmas. Geochim. Cosmochim. Acta 143, 8–22.

Li, H.K., 2020. Study on the Geological Structure and Superimposed Characteristics of Sichuan Basin. PhD thesis. Chengdu University of Technology (in Chinese with English abstract).

Li, C.F., Li, X.H., Li, Q.L., Guo, J.H., Yang, Y.H., 2012. Rapid and precise determination of Sr and Nd isotopic ratios in geological samples from the same filament loading by

thermal ionization mass spectrometry employing a single-step separation scheme. Anal. Chim. Acta 727, 54–60.

Li, H.B., Zhang, Z.C., Ernst, R., Lu, L.S., Santosh, M., Zhang, D.Y., Cheng, Z.G., 2015. Giant radiating mafic dyke swarm of the Emeishan Large Igneous Province, Identifying the mantle plume centre. Terra Nova 27 (4), 247–257.

Li, H.B., Zhang, Z.C., Santosh, M., Lü, L.S., Han, L., Liu, W., Cheng, Z.G., 2016. Late Permian basalts in the northwestern margin of the Emeishan Large Igneous Province, Implications for the origin of the Songpan-Ganzi terrane. Lithos 256–257, 75–87.

Li, H.B., Zhang, Z.C., Santosh, M., Lü, L.S., Han, L., Liu, W., 2017. Late Permian basalts in the Yanghe area, eastern Sichuan Province, SW China: implications for the geodynamics of the Emeishan flood basalt province and Permian global mass extinction. J. Asian Earth Sci. 134, 293–308.

Li, S.Z., Li, X.Y., Wang, G.Z., Liu, Y.M., Wang, Z.C., Wang, T.S., Cao, X.Z., Guo, X.Y., Somerville, I., Li, Y., Zhou, J., Dai, L.M., Jiang, S.H., Zhao, H., Wang, Y., Wang, G., Yu, S., 2019. Global Meso-Neoproterozoic plate reconstruction and formation mechanism for Precambrian basins: Constraints from three cratons in China. Earth Sci. Rev. 198 https://doi.org/10.1016/j.earscirev.2019.102946.

Li, X.J., Gu, Z.Y., Yong, Z.Q., Pan, F., Chen, H., Dong, X., Wu, Q.J., 2020. Reservoir characteristics, volcanic lithofacies cycles of Emeishan basalt in well Ys1, western Sichuan Basin. Mineral. Petrol. 40 (1), 100–112 (in Chinese with English abstract).

Liao, B.L., Zhang, Z.C., Kou, C.H., Li, H.B., 2012. Geochemistry of the Shuicheng Permian sodium trachybasalts in Guizhou Province and constraints on the mantle sources. Acta Petrol. Sin. 28 (4), 1238–1250 (in Chinese with English abstract).

Liu, K.L., Yang, S., Chen, H.D., Li, Q., Ma, L., Zhang, C.G., 2020. Characteristics and evolution of Permian volcanic rocks in Huayingshan area, eastern Sichuan province. Mineral. Petrol. 40 (1), 37–49 (in Chinese with English abstract).

Liu, S.G., Yang, Y., Deng, B., Zhong, Y., Wen, L., Sun, W., Li, Z.W., Jansa, L., Li, J.X., Song, J.M., Zhang, X.H., Peng, H.L., 2021. Tectonic evolution of the Sichuan Basin, Southwest China. Earth Sci. Rev. 213 https://doi.org/10.1016/j.earscirev.2020.103470.

Lu, J.L., Zuo, Z.X., Shi, Z., Dong, X., Wu, Q.J., Song, X.B., 2019. Characteristics of Permian volcanism in the western Sichuan Basin and its natural gas exploration potential. Nat. Gas Ind. 39 (02), 46–53 (in Chinese with English abstract).

Luttinen, A.V., Furnes, H., 2000. Flood basalts of Vestfjella: Jurassic magmatism across an Archaean-Proterozoic lithospheric boundary in Dronning Maud Land, Antarctica. J. Petrol. 41, 1271–1305.

Luttinen, A.V., Rämö, O.T., Huhma, H., 1998. Neodymium and strontium isotopic and trace element composition of a Mesozoic CFB suite from Dronning Maud Land, Antarctica: implications for lithosphere and asthenosphere contributions to Karoo magmatism. Geochim. Cosmochim. Acta 62, 2701–2714.

Ma, C.Q., Ehlers, C., Xu, C.H., 2000. The roots of the Dabieshan ultrahigh-pressure metamorphic terrain: constraints from geochemistry and Nd-Sr isotope systematics. Precambrian Res. 102, 279–301.

Ma, L., Jiang, S.-Y., Hou, M.-L., Dai, B.-Z., Jiang, Y.-H., Yang, T., Zhao, K.-D., Pu, W., Zhu, Z.-Y., Xu, B., 2014. Geochemistry of Early Cretaceous calc-alkaline lamprophyres in the Jiaodong Peninsula: implication for lithospheric evolution of the eastern North China Craton. Gondwana Res. 25, 859–872.

Ma, X.H., Li, G.H., Ying, D.L., Zhang, B.J., Li, Y., Dai, X., Fan, Y., Zeng, Y.X., 2019. Distribution and gas-bearing properties of Permian igneous rocks in Sichuan Basin, SW China. Pet. Explor. Dev. 46 (02), 216–225 (in Chinese with English abstract).

Marzoli, A., Callegaro, S., Dal Corso, J., Davies, J.H., Chiaradia, M., Youbi, N., Jourdan, F., 2018. The Central Atlantic Magmatic Province (CAMP): A Review. The Late Triassic World, pp. 91–125.

McKenzie, D., 1989. Some remarks on the movement of small melt fractions in the mantle. Earth Planet. Sci. Lett. 95, 53–72.

McKenzie, D., Bickle, M.J., 1988. The volume and composition of melt generated by extension of the Lithosphere. J. Petrol. 29, 625–679.

McKenzie, D.P., O'Nions, R.K., 1991. Partial melt distribution from inversion of rare earth element concentrations. J. Petrol. 32, 1021–1991.

McKenzie, D.P., O'Nions, R.K., 1995. The source regions of ocean island basalts. J. Petrol. 36, 133–159.

Metcalfe, I., 2013. Gondwana dispersion and Asian accretion: tectonic and palaeogeographic evolution of eastern Tethys. J. Asian Earth Sci. 66, 1–33.

Millett, J.M., Hole, M.J., Jolley, D.W., Passey, S.R., 2017. Geochemical stratigraphy and correlation within large igneous provinces: the final preserved stages of the Faroe Islands Basalt Group. Lithos 286, 1–15.

Mollo, S., Blundy, J.D., Iezzi, G., Scarlato, P., Langone, A., 2013. The partitioning of trace elements between clinopyroxene and trachybasaltic melt during rapid cooling and crystal growth. Contrib. Mineral. Petrol. 166, 1633–1654.

Munteanu, M., Wilson, A.H., Costin, G., Yao, Y., Lum, J.E., Jiang, S.Y., Jourdan, F., Chunnett, G., Cioacă, M.E., 2017. The mafic–ultramafic dykes in the Yanbian Terrane (Sichuan Province, SW China): record of magma differentiation and emplacement in the Emeishan large Igneous Province. J. Petrol. 58 (3), 513–538.

Niu, Y.L., Batiza, R., 1991. An empirical method for calculating melt compositions produced beneath mid-ocean ridges: application for axis and off-axis (seamounts) melting. J. Geophys. Res. 96, 21753–21777.

O'Hara, M.J., 1977. Geochemical evolution during fractional crystallization of a periodically refilled magma chamber. Nature 266, 503–507.

Orejana, D., Villaseca, C., Paterson, B.A., 2008. Geochemistry of pyroxenitic and hornblenditic xenoliths in alkaline lamprophyres from the Spanish Central System. Lithos 86, 167–196.

Osborn, E.F., Tait, D.B., 1952. The system diopside-forsterite-anorthite. Am. J. Sci. 413–433.

Peate, I.U., Bryan, S.E., 2008. Re-evaluating plume-induced uplift in the Emeishan large igneous province. Nat. Geosci. 1 (9), 625–629.

Prelević, D., Foley, S.F., Romer, R.L., Conticelli, S., 2008. Mediterranean Tertiary lamproites derived from multiple source components in postcollisional geodynamics. Geochim. Cosmochim. Acta 72, 2125–2156.

Prelević, D., Jacob, D.E., Foley, S.F., 2013. Recycling plus: a new recipe for the formation of Alpine–Himalayan orogenic mantle lithosphere. Earth Planet. Sci. Lett. 362, 187–197.

Putirka, K.D., 2008. Thermometers and barometers for volcanic systems. Rev. Mineral. Geochem. 69, 61–120.

Qi, L., Zhou, M.F., 2008. Platinum-group elemental and Sr-Nd-Os isotopic geochemistry of Permian Emeishan flood basalts in Guizhou Province, SW China. Chem. Geol. 248, 83–103.

Qian, Q., Hermann, J., 2013. Partial melting of lower crust at 10–15 kbar: constraints on adakite and TTG formation. Contrib. Mineral. Petrol. 165 (6), 1195–1224.

Richards, M.A., Duncan, R.A., Courtillot, V.E., 1989. Flood basalts and hotspot tracks: plume heads and tails. Science 246, 103–108.

Rudnick, R.L., Gao, S., 2003. Composition of the continental crust. The Crust 2003 (3), 1–64.

Schoene, B., Samperton, K.M., Eddy, M.P., Keller, G., Adatte, T., Bowring, S.A., Khadri, S.F.R., Gertsch, B., 2015. U-Pb geochronology of the Deccan Traps and relation to the end-Cretaceous mass extinction. Science 347, 182–184.

Sen, G., 2001. Generation of Deccan trap magmas. J. Earth Syst. Sci. 110 (4), 409–431.

Shellnutt, J.G., 2014. The Emeishan large igneous province: a synthesis. Geosci. Front. 5, 369–394.

Shellnutt, J.G., Denyszyn, S.W., Mundil, R., 2012. Precise age determination of mafic and felsic intrusive rocks from the Permian Emeishan large igneous province (SW China). Gondwana Res. 22, 118–126.

Shellnutt, J.G., Jahn, B.M., 2011. Origin of Late Permian Emeishan basaltic rocks from the Panxi region (SW China): implications for the Ti-classification and spatial–compositional distribution of the Emeishan flood basalts. J. Volcanol. Geotherm. Res. 199 (1–2), 85–95.

Shellnutt, J.G., Pham, T.T., Denyszyn, S.W., Yeh, M.W., Tran, T.A., 2020. Magmatic duration of the Emeishan large igneous province: insight from northern Vietnam. Geology 48 (5), 457–461.

Søager, N., Holm, P.M., 2011. Changing compositions in the Iceland plume; isotopic and elemental constraints from the Paleogene Faroe flood basalts. Chem. Geol. 280 (3–4), 297–313.

Sobolev, S.V., Sobolev, A.V., Kuzmin, D.V., Krivolutskaya, N.A., Petrunin, A.G., Arndt, N.T., Radko, V.A., Vasiliev, Y.R., 2011. Linking mantle plumes, large igneous provinces and environmental catastrophes. Nature 477 (7364), 312-31 6.

Spera, F.J., Bohrson, W.A., 2001. Energy-constrained open-system magmatic processes I: general model and energy-constrained assimilation and fractional crystallization (EC-AFC) formulation. J. Petrol. 42, 999–1018.

Sun, S.S., McDonough, W.F., 1989. Chemical and isotopic systematics of oceanic basalt: implications for mantle composition and processes. In: Sanders, A.D., Norry, M.J. (Eds.), Magmatism in the Ocean Basins 42. Geological Society Special Publication, London, pp. 313–345.

Sun, C., Graff, M., Liang, Y., 2017. Trace element partitioning between plagioclase and silicate melt: the importance of temperature and plagioclase composition, with implications for terrestrial and lunar magmatism. Geochim. Cosmochim. Acta 206, 273–295.

Svensen, H., Planke, S., Polozov, A.G., Schmidbauer, N., Corfu, F., Podladchikov, Y.Y., Jamtveit, B., 2009. Siberian gas venting and the end-Permian environmental crisis. Earth Planet. Sci. Lett. 277 (3–4), 490–500.

Tanaka, T., Togashi, S., Kamioka, H., Amakawa, H., Kagami, H., Hamamoto, T., et al., 2000. Jndi-1: a neodymium isotopic reference in consistency with lajolla neodymium. Chem. Geol. 168 (168), 279–281.

Thirlwall, M.F., 1991. Long-term reproducibility of multicollector sr and nd isotope ratio analysis. Chem. Geol. 94 (2), 85–104.

Tian, J.C., Lin, X.B., Guo, W., Zhang, X., Huang, P.H., 2017. Geological significance of oil and gas in the Permian basalt eruption event in Sichuan Basin, China. J. Chengdu Univ. Technol. 44 (01), 14–20.

Wang, Y.J., Fan, W.M., Zhang, Y.H., Guo, F., Zhang, H.F., Peng, T.P., 2004. Geochemical, 40Ar/39Ar geochronological and Sr-Nd isotopic constraints on the origin of Paleoproterozoic mafic dikes from the southern Taihang Mountains and implications for the ca. 1800Ma event of the North China Craton. Precambrian Res. 135, 55–77.

Wang, C.Y., Zhou, M.F., Qi, L., 2007. Permian flood basalts and mafic intrusions in the Jinping (SW China)-Song Da (northern Vietnam) district: mantle sources, crustal contamination and sulfide segregation. Chem. Geol. 243, 317–343.

Wang, Z.H., Chen, Y., Chen, L., Song, H.B., 2018. Thermal-rheological effects induced by crustal magmatic underplating and implications for Emeishan Large Igneous Province. Acta Petrol. Sin. 34 (01), 91–102.

Weaver, B.L., 1991. The origin of ocean island basalt end-member compositions: trace element and isotopic constraints. Earth Planet. Sci. Lett. 104, 381–397.

Weis, D., Kieffer, B., Maerschalk, C., Pretorius, W., Barling, J., 2005. High-precision Pb-Sr-Nd-Hf isotopic characterization of USGS BHVO-1 and BHVO-2 reference materials. Geochem. Geophys. Geosyst. 6 (2).

Weis, D., Kieffer, B., Maerschalk, C., Barling, J., Jong, J.D., Williams, G.A., et al., 2006. High-precision isotopic characterization of USGS reference materials by TIMS and MC-ICP-MS. Geochem. Geophys. Geosyst. 7 (8), 139–149.

Wignall, P.B., Sun, Y., Bond, D.P.G., Izon, G., Newton, R.J., Vedrine, S., Widdowson, M., Ali, J.R., Lai, X., Jiang, H., Cope, H., Bottrell, S.H., 2009. Volcanism, mass extinction, and carbon isotope fluctuations in the middle Permian of China. Science 324, 1179–1182.

Willbold, M., Stracke, A., 2006. Trace element composition of mantle end-members: implications for recycling of oceanic and upper and lower continental crust. Geochem. Geophys. Geosyst. 7 (4).

Wilson, M., 1989. Igneous Petrogenesis. Unwin Hyman, London, p. 466.

Winchester, J.A., Floyd, P.A., 1977. Geochemical discrimination of different magma series and their differentiation products using immobile elements. Chem. Geol. 20, 325–343.

Workman, R.K., Hart, S.R., 2005. Major and trace element composition of the depleted MORB mantle (DMM). Earth Planet. Sci. Lett. 231 (1–2), 53–72.

Xia, M.L., Wen, L., Li, Y., Luo, B., He, K.L., Liu, R., Qiu, Y.C., He, Q.L., Chen, K., 2020. Permian volcanic eruption cycle, environment and model in the Jianyang area of the Sichuan Basin. Nat. Gas Ind. 40 (09), 11–22 (in Chinese with English abstract).

Xiao, L., Xu, Y.G., Mei, H.J., Zheng, Y.F., He, B., Pirajno, F., 2004. Distinct mantle sources of low-Ti and high-Ti basalts from the western Emeishan large igneous provinces, SW China: implications of plume lithosphere interaction. Earth Planet. Sci. Lett. 228, 525–546.

Xiong, X.S., Gao, R., Zhang, J.S., Wang, H.Y., Guo, L.H., 2015. Differences of structure in mid-lower crust between the eastern and western blocks of the Sichuan Basin. Chin. J. Geophys. 58 (07), 2413–2423 (in Chinese with English abstract).

Xu, Y.G., Chung, S.L., Jahn, B.M., Wu, G., 2001. Petrologic and geochemical constraints on the petrogenesis of Permian-Triassic Emeishan flood basalts in southwestern China. Lithos 58, 145–168.

Xu, Y.G., He, B., Chung, S.L., Menzies, M.A., Frey, F.A., 2004. Geologic, geochemical, and geophysical consequences of plume involvement in the Emeishan flood-basalt province. Geology 32, 917.

Xu, Y.G., He, B., Huang, X.L., Luo, Z.Y., Zhu, D., Ma, J.L., Shao, H., 2007. Late Permian Emeishan flood basalts in southwestern China. Earth Sci. Front. 14 (2), 1–9.

Xu, Q., Qiu, N.S., Liu, W., Shen, A.J., Wang, X.F., 2018. Thermal evolution and maturation of Sinian and Cambrian source rocks in the central Sichuan Basin, Southwest China. J. Asian Earth Sci. 164, 143–158.

Xu, J., Xia, X.P., Cai, K., Lai, C.K., Liu, X.J., Yang, Q., Zhou., M.F., Ma, P.F., Zhang, L., 2020. Remnants of a Middle Triassic island arc on western margin of South China Block: evidence for bipolar subduction of the Paleotethyan Ailaoshan Ocean. Lithos 360, 105447.

Yang, Y.M., Yang, Y., Wen, L., Zhang, X.H., Chen, C., Chen, K., Zhang, Y., Di, G.F., Wang, H., Xie, C., 2020. New exploration progress and prospect of Middle Permian natural gas in the Sichuan Basin. Nat. Gas Ind. 41 (01), 42–58 (in Chinese with English abstract).

Yang, Y.M., Chen, Y.L., Liu, S.Y., Deng, B., Xu, H., Chen, L.Q., Li, D.Y., Yin, Y.Z., Li, Y., 2021. Status, potential and prospect of shale gas exploration and development in the Sichuan Basin and its periphery. Nat. Gas Ind. 41 (01), 42–58 (in Chinese with English abstract).

Yao, J.H., Zhu, W.G., Wang, Y.J., Zhong, H., Bai, Z.J., 2021. Geochemistry of the Yumen picrites-basalts from the Emeishan large igneous province: implications for their mantle source, PGE behaviors, and petrogenesis. Lithos 400–401, 106364.

Zhang, J.L., 2008. The Sr-Nd-Pb Isotopic Geochemistry of Kongling High-grade terrain of the Yangtze Craton (South China) and Its Tectonic Implications. China University of Geoscience (in Chinese with English abstract).

Zhang, G.W., Meng, Q.R., Yu, Z.P., Sun, Y., Zhou, D.W., Guo, A.L., 1996. Orogenesis and dynamics of the Qinling Orogen. Sci. China Earth Sci. 39 (3), 193–200 (in Chinese with English abstract).

Zhang, G.W., Dong, Y.P., Lai, S.C., Guo, A.L., Meng, Q.R., Liu, S.F., Chen, S.Y., Yao, A.P., Zhang, Z.Q., Pei, X.Z., Li, S.Z., 2003. Mianlue tectonic zone and Mianlue suture zone in southern margin of Qinling Dabie orogenic belt. Sci. China Earth Sci. 33 (12), 1122–1135 (in Chinese with English abstract).

Zhang, Z.C., Mahoney, J.J., Mao, J.W., Wang, F.S., 2006. Geochemistry of picritic and associated basalt flows of the western Emeishan flood basalt province, China. J. Petrol. 47, 1997–2019.

Zhang, Z.C., Zhi, X.C., Chen, L.L., Saunders, A.D., Reichow, M.K., 2008. Re-Os isotopic compositions of picrites from the Emeishan flood basalt province, China. Earth Planet. Sci. Lett. 276 (1–2), 30–39.

Zhang, Z.C., Mao, J.W., Saunders, A.D., Ai, Y., Li, Y., Zhao, L., 2009. Petrogenetic modeling of three mafic-ultramafic layered intrusions in the Emeishan large igneous province, SW China, based on isotopic and bulk chemical constraints. Lithos 113 (3–4), 369–392.

Zhang, G.W., Guo, A.L., Wang, Y.J., Li, S.Z., Dong, Y.P., Liu, S.F., He, D.F., Cheng, S.Y., Lu, R.K., Yao, A.P., 2013. Tectonics of South China continent and its implications. Sci. China Earth Sci. 43 (10), 1804–1828 (in Chinese with English abstract).

Zhang, G.J., Zhang, X.L., Li, D.D., Farquhar, J., Shen, S.Z., Chen, X.Y., Shen, Y.N., 2015. Widespread shoaling of sulfidic waters linked to the end-Guadalupian (Permian) mass extinction. Geology 43 (12), 1091–1094.

Zhang, L., Ren, Z.Y., Handler, M.R., Wu, Y.D., Zhang, L., Qian, S.P., Xia, X.P., Yang, Q., Xu, Y.G., 2019. The origins of high-Ti and low-Ti magmas in large igneous provinces, insights from melt inclusion trace elements and Sr-Pb isotopes in the Emeishan large Igneous Province. Lithos 344, 122–133.

Zhao, G.C., Wang, Y.J., Huang, B.C., Dong, Y.P., Li, S.Z., Zhang, G.W., Yu, S., 2018. Geological reconstructions of the East Asian blocks: from the breakup of Rodinia to the assembly of Pangea. Earth Sci. Rev. 186, 262–286.

Zhong, Y.T., He, B., Mundil, R., Xu, Y.G., 2014. CA-TIMS zircon U-Pb dating of felsic ignimbrite from the Binchuan section: implications for the termination age of Emeishan large igneous province. Lithos 204, 14–19.

Zhou, M.F., Robinson, P.T., Lesher, C.M., Keays, R.R., Zhang, C.J., Malpas, J., 2005. Geochemistry, petrogenesis and metallogenesis of the Panzhihua gabbroic layered intrusion and associated V–Ti–Fe oxide deposits, Sichuan Province, SW China. J. Petrol. 46, 2253–2280.

Zhou, M.F., Arndt, N.T., Malpas, J., Wang, C.Y., Kennedy, A.K., 2008. Two magma series and associated ore deposit types in the Permian Emeishan large igneous province, SW China. Lithos 103 (3–4), 352–368.

Zhu, C.Q., Xu, M., Yuan, Y.S., Zhao, Y.Q., Shan, J.N., He, Z.G., Tian, Y.T., Hu, S.B., 2010. Palaeogeothermal response and record of the effusing of Emeishan basalts in the Sichuan basin. Chin. Sci. Bull. 55, 949–956 (in Chinese with English abstract).

Zhu, C.Q., Hu, S.B., Qiu, N.S., Rao, S., Yuan, Y.S., 2016. The thermal history of the Sichuan Basin, SW China: evidence from the deep boreholes. Sci. China Earth Sci. 59, 70–82 (in Chinese with English abstract).

Zhu, C.Q., Hu, S.B., Qiu, N.S., Jiang, Q., Rao, S., Liu, S., 2018a. Geothermal constraints on Emeishan mantle plume magmatism: paleotemperature reconstruction of the Sichuan Basin, SW China. Int. J. Earth Sci. 107 (1), 71–88.

Zhu, J., Zhang, Z.C., Reichow, M.K., Li, H.B., Cai, W.C., Pan, R.H., 2018b. Weak vertical surface movement caused by the ascent of the Emeishan mantle anomaly. J. Geophys. Res. Solid Earth 123, 1018–1034.

Zhu, J., Zhang, Z.C., Santosh, M., Tan, S.C., Deng, Y.N., Xie, Q.H., 2021a. Recycled carbon degassed from the Emeishan plume as the potential driver for the major end-Guadalupian carbon cycle perturbations. Geosci. Front. 12 (4) https://doi.org/10.1016/j.gsf.2021, 101140.

Zhu, J., Zhang, Z.C, Santosh, M., Tan, S.C., Jin, Z.L., 2021b. Submarine basaltic eruptions across the Guadalupian-Lopingian transition in the Emeishan large igneous province: implication for end-Guadalupian extinction of mar.ine biota. Gondwana Res., 92, 228–238.

Zindler, A., Hart, S., 1986. Chemical geodynamics. Annu. Rev. Earth Planet. Sci. 14, 493–571.

Zou, C.N., Du, J.H., Xu, C.C., 2014. Formation, distribution, resource potential and discovery of the Sinian−Cambrian giant gas field, Sichuan Basin, SW China. Pet. Explor. Dev. 41 (03), 278–293 (in Chinese with English abstract).